REPORT DOCUMENTATION PAGE

Form Approved
OMB No. 0704-0188

1. AGENCY USE ONLY (Leave blank)	2. REPORT DATE	3. REPORT TYPE AND DATES COVERED
	30 November 95	Final Technical 4/1/92 – 9/30/94

4. TITLE AND SUBTITLE
Experimental Research on Crossing Shock Wave Boundary Layer Interactions

6. AUTHOR(S)
G.S. Settles and T.J. Garrison

5. FUNDING NUMBERS
AFOSR-89-0315
2307/AS

7. PERFORMING ORGANIZATION NAME(S) AND ADDRESS(ES)
Prof. Gary S. Settles, Director
Penn State Gas Dynamics Laboratory
Dept. of Mechanical Engineering
301D Reber Bldg.
University Park, PA 16802

DTIC ELECTE FEB 17 1995 S G D

8. PERFORMING ORGANIZATION REPORT NUMBER
AFOSR-TR- 195- 0073

9. SPONSORING/MONITORING AGENCY NAME(S) AND ADDRESS(ES)
AIR FORCE OFFICE OF SCIENTIFIC RESEARCH
DIRECTORATE OF AEROSPACE SCIENCES
BOLLING AFB, DC 20332-6448

NA

10. SPONSORING/MONITORING AGENCY REPORT NUMBER
AFOSR-89-0315

11. SUPPLEMENTARY NOTES

19950207 064

12a. DISTRIBUTION/AVAILABILITY STATEMENT

APPROVED FOR PUBLIC RELEASE
DISTRIBUTION IS UNLIMITED

12b. DISTRIBUTION CODE

13. ABSTRACT (Maximum 200 words)
An experimental research effort of the Penn State Gas Dynamics Laboratory on the subject of crossing shock wave boundary layer interactions is reported. This three year study was supported by AFOSR Grant 89-0315. A variety of experimental techniques were employed to study the above phenomena including planar laser scattering flowfield visualization, kerosene lampblack surface flow visualization, laser interferometer skin friction surveys, wall static pressure measurements, and flowfield five-hole probe surveys. For a model configuration producing two intersecting shock waves, measurements were made for a range of oblique shock strengths at freestream Mach numbers of 3.0 and 3.85. Additionally, measurements were made at Mach 3.85 for a configuration producing three intersecting waves. The combined experimental dataset was used to formulate the first detailed flowfield models of the crossing-shock and triple-shock wave/boundary layer interactions. The structure of these interactions was found to be similar over a broad range of interaction strengths and is dominated by a large, separated, viscous flow region.

14. SUBJECT TERMS Crossing Shock Wave Interactions, Interactional Aerodynamics, Compressible Boundary Layers, Turbulent Boundary Layers, Supersonic Wind Tunnels, Flow Visualization	15. NUMBER OF PAGES 26
	16. PRICE CODE

17. SECURITY CLASSIFICATION OF REPORT	18. SECURITY CLASSIFICATION OF THIS PAGE	19. SECURITY CLASSIFICATION OF ABSTRACT	20. LIMITATION OF ABSTRACT
UNCLASSIFIED	UNCLASSIFIED	UNCLASSIFIED	

NSN 7540-01-280-5500

Standard Form 298 (Rev. 2-89)
Prescribed by ANSI Std. 239-18

Department of Mechanical Engineering
Pennsylvania State University
University Park, PA 16802

Experimental Research on Crossing Shock Wave/Boundary Layer Interactions

By

G.S. Settles and T.J. Garrison

Final Technical Report for the Period 1 April 1991 to 30 September 1994 on Grant AFOSR-89-0315

Accesion For		
NTIS CRA&I	X	
DTIC TAB	☐	
Unannounced	☐	
Justification		
By		
Distribution /		
Availability Codes		
Dist	Avail and / or Special	
A-1		

Submitted to:

Dr. Leonidas Sakell, Program Manager
US Air Force Office of Scientific Research
Bldg. 410, Bolling AFB, DC 20332-6448

October 30, 1994

DTIC QUALITY INSPECTED 4

PSU Gas Dynamics Laboratory

TABLE OF CONTENTS

I. SUMMARY

This report documents the results of a three-year experimental study conducted at the Penn State Gas Dynamics Laboratory to investigate the flowfield structure created by crossing oblique shock waves interacting with a turbulent boundary layer. Such interactions are of practical importance in the design of high-speed inlets. A variety of experimental techniques were employed to study the crossing-shock wave/boundary layer interactions including planar laser scattering flowfield visualization, kerosene lampblack surface flow visualization, laser interferometer skin friction surveys, wall static pressure measurements, and flowfield five-hole probe surveys. For a model configuration producing two intersecting shock waves, measurements were made for a range of oblique shock strengths at freestream Mach numbers of 3.0 and 3.85. Additionally, measurements were made at Mach 3.85 for a configuration producing three intersecting waves. The combined experimental dataset was used to formulate the first detailed flowfield models of the crossing-shock and triple-shock wave/boundary layer interactions. The structure of these interactions was found to be similar over a broad range of interaction strengths and is dominated by a large, separated, viscous flow region.

II. INTRODUCTION

The interaction between crossing oblique shock waves and a turbulent boundary layer is a fundamental viscous/inviscid fluid dynamics problem with many practical applications. In particular, the applications include the aerodynamics of a variety of airbreathing engine inlets as well as that of finned bodies. While a great deal of research has been directed toward understanding shock wave/boundary layer interactions, the majority of this research has been concerned with 2-D and very simple 3-D interactions. More complicated interactions, such as the crossing-shock and triple-shock interactions, have only recently begun to receive significant attention. The study of these interactions represents a logical progression in the effort to understand shock/boundary layer interactions; these interactions represents fully 3-D flows that are made up of basic single-shock flows for which a great deal has been learned. Also, the experimental data obtained as part of this study will serve as a benchmark for CFD code validation within a complex flowfield. Figures 1 and 2 show a schematic of the test models used for the crossing-shock and triple-shock experiments, respectively.

Prior to the subject research program very little was known about the crossing-shock or triple-shock interactions. While several prior studies had been performed for the crossing-shock configuration, these studies focused on measurement of surface pressure and surface streamline patterns[1-6] and no data were taken *within* the flowfield. Additionally, several computed solutions had been obtained but could not be validated due to a lack of experimental data.[7-9]

Although the early studies provided a good first step, they only scratched the surface in the overall study of these interactions. Some of the key issues in the study of crossing-shock interactions at this point in time (August, 1990) were: (1) no understanding of the flowfield physics governing these interactions had been established; (2) there was a definite need for more experimental data for use in understanding the flows as well as validating the computations, especially data within the outer flowfield and data that would provide stringent tests of the turbulence models used; and (3) only a limited range of interaction strengths had been investigated, with most of the available data being for relatively weak interactions.

These issues led to the formation of current research program, funded by The Air Force Office of Scientific Research (AFOSR). An experimental program was set up at The Penn State University Gas Dynamics Laboratory to examine supersonic crossing-shock and triple-shock interactions over a broad range of interaction strengths. Companion computational programs were initiated at NASA-Ames and Rutgers University to compute selected flows studied at Penn State.

This Final Technical Report summarizes the crossing-shock and triple-shock wave/boundary layer interaction research program conducted at Penn State University under AFOSR Grant 89-0315. The objective of the research program was to develop a fundamental understanding of the flowfield physics governing these interactions via a combination of experimental flowfield visualizations and measurements coupled with a comparison to available computational results. The work summarized herein was performed during the period from 1 April 1991 to 30 September 1994. A list of publications resulting from this work is given in Section VII.

III. EXPERIMENTAL METHODS

Facility and Test Conditions

The experiments were performed in the Penn State Gas Dynamics Laboratory's Supersonic Wind Tunnel Facility, which is an intermittent blowdown tunnel with a test section size of 15x17x60 cm. This facility has a unique variable Mach number capability over the range from Mach 1.5 to 4.0 by way of an asymmetric sliding block nozzle.

Figure 1 shows the model geometry used for the crossing-shock experiments. This model consists of two vertical fins, at angles of attack α_1 and α_2, mounted on a horizontal flat plate. The flat plate generates an equilibrium, nearly-adiabatic, zero-pressure-gradient turbulent boundary layer which interacts with the two crossing oblique shock waves generated by the fins.

The model geometry used for the triple-shock experiments is given in Figure 2. In this model, a third oblique shock wave is produced by adding a compression ramp of angle ϕ between the two vertical fins. The leading edge of this compression ramp is coincident with that of the fins.

A variety of flow diagnostic techniques were used to study the interactions created by the geometries shown in Figures 1 and 2. Table 1 summarizes the complete test matrix examined in the subject research program. Crossing-shock experiments were performed at freestream Mach numbers, M_∞, of 3.0 and 3.85 for a range of symmetric and asymmetric fin angles from 7 to 13 degrees at Mach 3 and from 7 to 15 degrees at Mach 3.85. The triple shock experiments were performed for a single case at $M_\infty = 3.85$ with $\alpha_1 = \alpha_2 = 15°$ and $\phi = 10°$. The experimental techniques included kerosene lampblack surface flow visualization, Planar Laser Scattering (PLS) flowfield visualization, wall static pressure measurements, Laser Interferometer Skin Friction (LISF) measurements, and 5-hole probe flowfield surveys. The model configuration and test conditions for which each technique was applied is noted in Table 1. An overview of the experimental techniques is given in the following subsections.

Kerosene Lampblack Surface Flow Visualizations

The details of the limiting wall streamline patterns (i.e. the interaction "footprint") were made visible using the kerosene lampblack method.[10] In this method, a mixture of kerosene and lampblack is applied to the test model prior to testing. During the course of the wind tunnel run,

Table 1: Experimental Test Matrix

Model Configuration	M_∞	α_1	α_2	ϕ	PLS flow vis.	Kerosene Lampblack	P_{wall}	LISF wall shear, C_f	5-hole probe surveys
Symmetric Crossing -Shock	3	7	7	—	✓	✓	✓	✓	
		9	9	—	✓	✓	✓		
		11	11	—	✓	✓	✓	✓	
		13	13	—	✓	✓	✓		
	3.85	7	7	—	✓	✓	✓		
		9	9	—	✓	✓	✓		
		11	11	—	✓	✓	✓		
		13	13	—	✓	✓	✓		
		15	15	—	✓	✓	✓	✓	✓
Asymmetric Crossing-Shock	3.85	7	15	—	✓	✓			
		9	15	—	✓	✓			
		11	15	—	✓	✓			
		13	15	—	✓	✓			
Triple-Shock	3.85	15	15	10	✓	✓			

the mixture flows over the model surface and the kerosene evaporates, leaving only the lamp-black pigment on the model surface. This lampblack pattern is then removed from the model surfaces using large sections of matte adhesive tape, thus permanently preserving the pattern. Further details of the method as used in the crossing-shock study are given in Reference 11.

Planar Laser Scattering Flowfield Visualizations

Planar Laser Scattering (PLS) visualization, also known as laser-light-screen or vapor-screen visualization, was used to non-intrusively observe the crossing-shock and triple-shock flowfield structure. In this technique, a laser beam is formed into a thin sheet and passed through the flowfield of interest. Seed particles within the flow scatter the laser light as they pass through the sheet; thus, the scattered light intensity is related to the flow density. By recording the scattered light on a CCD camera, images of the flowfield structure can be obtained.

In the Penn State Supersonic Wind Tunnel facility, ice crystals are used as seed particles for the PLS visualization. By partially bypassing the silica gel dryer, a slight amount of moisture is allowed in the stored air supply. During the expansion process through the convergent-divergent wind tunnel nozzle, this moisture condenses and freezes into ice crystals. The ice crystals formed during this process have been measured to be 0.2 to 0.3 μm in diameter, which is sufficient for the particles to accurately track the flow.

Because it reveals the flow structure only within the plane of the light sheet, the PLS technique is extremely powerful for visualizing complex three-dimensional flows. For the visualizations of the crossing-shock and triple-shock flows, the entire interaction structure was visualized by traversing the light sheet from the fin leading to trailing edges. By sweeping the sheet through the entire flow, a tomographical view of the flowfield was constructed. Further details on the PLS technique and the configuration used to visualize the crossing-shock flows are given in References 11-13.

Wall Static Pressure Measurements

The static pressure taps used for the subject experiments were located along a single row extending down the centerline of the symmetric crossing-shock interaction. A total of 40 static taps were placed in the plate surface. The coordinates of the taps relative to the model geometry are documented in Reference 11.

Laser Interferometer Skin Friction Measurements

As noted in Table 1, skin friction measurements were made on the flat plate surface for a weak, moderate, and strong crossing-shock interaction. The wall shear measurements were obtained using a Laser Interferometer Skin Friction (LISF) meter. The basic principle of operation of the LISF meter is to optically measure the time rate of thinning of an oil film placed on a test surface subject to aerodynamic shear. The rate of thinning of the oil film is determined using optical interference and can be related to the applied shear through lubrication theory. In this way, the shear stress can be determined without any knowledge of the overlying flow properties (i.e., only the properties of the oil and not the properties of the outer flow are required to determine the shear).

As part the subject AFOSR grant, the LISF instrument and data reduction-algorithm were revised and enhanced to improve its operation in complex, high-speed flows such as the crossing-shock interaction. It was found that shear stresses up to 700 N/m^2 could be successfully

measured using the LISF technique. Further details on the LISF instrument are given in References 11 and 14.

5-Hole Probe Flowfield Surveys

Flowfield surveys within the crossing-shock interaction were made using a recently-developed fast-response five-hole probe. (Details of the probe design are given by in Ref. 15.) The outputs of the five-hole probe are the local Mach number, M, pitot pressure, P_p, pitch and yaw angles, ϕ and ψ, respectively, and the static and stagnation pressures, P and P_t. The probe is designed for measurements over the Mach number range from 1.5 to 4.0 with typical errors of $\pm$ 5%. To make surveys of the crossing-shock flowfield, the probe was mounted in a sting connected to a traverse system installed in the diffuser section of the wind tunnel. The traverse system consisted of two linear screw traverses driven by computer controlled stepper motors. The linear traverses provided controlled movement of the probe in the X and Y coordinate directions, thus enabling the probe to survey X-Y planes at a variety of preset Z locations (coordinate directions are given in Fig. 1).

The probe surveys of the crossing-shock interaction were performed at two Z planes for the strongest crossing-shock interaction (see Table 1). At each of the survey planes, an array of measurements was taken on an equally spaced grid with 1 mm increments in both the X and Y directions. Because the measurements were made for a symmetric crossing-shock interaction, only half the interaction was surveyed at each Z plane. (The symmetry of the interaction was first verified through a limited set of surveys made on either side of the plane of symmetry.) Further detail on the experimental configuration used in the probe surveys can be found in References 11 and 16.

IV. RESEARCH ACCOMPLISHMENTS

During the three year period covered by the subject AFOSR grant, a significant number of research accomplishments were made, greatly enhancing the understanding of the crossing-shock and triple-shock interactions. As listed in section VII, a number of publications have resulted from the research program which discuss in detail the important observations and conclusions drawn from the program. Hence, rather than reiterate the content of those papers herein, the intent of this section is to summarize the key results drawn from the research program and to provide the appropriate references for obtaining additional details.

Planar Laser Scattering Visualizations

This section focuses on the results of the PLS visualizations for the symmetric crossing-shock interactions listed in Table 1. Results for the asymmetric crossing-shock cases and the triple-shock interaction are given in later sections.

PLS images were obtained for all the symmetric crossing-shock interactions listed in Table 1. Figure 3 shows a sequence of 14 PLS images of the Mach 3.85, $\alpha_1 = \alpha_2 = 15°$ interaction. These images, discrete frames extracted from the complete PLS visualization, correspond to a series of slices throughout the flowfield. Figure 4 shows the locations of the slices relative to the model geometry and inviscid shock waves. Each image is to scale and is as seen by an observer located downstream of the interaction and looking upstream (ie the freestream flow is out of the page). The first image occurs at a normalized streamwise coordinate of $Z/\delta_\infty = 16.6$ and the

spacing between subsequent frames is $\Delta Z/\delta_\infty = 1.43$ where $\delta_\infty = 3.5$ mm. The location of the flat plate surface is marked in frame (a) of Figure 3.

Flowfield images, such as those shown in Figure 3, proved extremely valuable in determining the structure of the crossing-shock interaction. The images clearly show the shock waves within the flowfield, which appear as sharp intensity changes in the images. Additionally, the PLS images show the general shape and location of the boundary layer and separated flow region; they appear as dark areas in the PLS visualizations due to extinction of the ice crystals by the elevated temperatures therein.

By extracting the key features shown in the PLS images of Figure 3, a detailed flowfield model of the symmetric crossing-shock interaction was developed. This model is shown in Figure 5. (Only half of the interaction is shown in the model since it was developed for a symmetric crossing-shock interaction.)

In developing the flowfield model, it proved useful to consider the symmetric crossing-shock interaction as an equivalent reflection of a single-fin interaction from a inviscid wall. Analyzing the flowfield in this manner showed that the crossing-shock interaction is formed by a complex, irregular crossing of two single-fin interactions. The resulting flowfield is comprised of a complex shock wave structure overlying a large, viscous, separated flow region. The effects of the viscous/inviscid interaction were found to extend a significant distance above the plate surface, illustrating the dominant effect which the viscous region imposes on the flowfield. The formation of the substantial separated flow region also raises important concerns for the use of the crossing-shock geometry as a high-speed inlet. A thorough discussion of all the features present in the flowfield model can be found in References 11 and 17.

Surface Flow Visualizations

Surface flow patterns obtained using the kerosene lampblack method were recorded for all the interaction cases shown in Table 1. Figure 6 shows two such patterns, one for a weak crossing-shock interaction at $M_\infty = 3$, $\alpha_1 = \alpha_2 = 7°$ and one for a strong interaction at $M_\infty = 3.85$, $\alpha_1 = \alpha_2 = 15°$. Analysis of all the recorded patterns shows that, for all but the weakest interaction (i.e., the $M_\infty = 3$, $\alpha_1 = \alpha_2 = 7°$ interaction), the entire incoming boundary layer separates from the plate surface. Once separated, the boundary layer fluid accumulates on the interaction centerline, forming the large viscous region observed in PLS images of Figures 3 and 5. As noted previously, the separation of the entire incoming boundary layer and its accumulation on the interaction centerline raises important concerns for the use of the crossing-shock geometry as a high-speed inlet.

Detailed descriptions of the intricate topological features present in the surface flow patterns are given in References 11 and 18.

Interaction Strength Effects

An important conclusion drawn from the PLS images and surface flow patterns was that the basic structure of the symmetric crossing-shock interaction is qualitatively similar over a broad range of interaction strengths. For all but the weakest case, the dominant features in the surface footprint and flowfield structure appeared in all the interactions. The primary effect of increasing the interaction strength was to increase both the strength of the various waves and the

size of the separated flow region. More detailed information on the evolution of the crossing-shock flowfield with increasing interaction strength is given in References 11 and 18.

Additionally, it is important to note that the surface flow patterns observed in recent studies of hypersonic interactions[19-24] at Mach 8.2 are qualitatively similar to the supersonic interactions studied herein. Hence, it appears that the crossing-shock flowfield may remain similar over a very broad range of interaction strengths.

Wall Pressure Measurements

The primary motivation for taking a limited set of wall pressure measurements was to link the current experiments with those of previous investigators who had already performed extensive wall pressure surveys.[2,4] For the current experiments, up to 40 wall static pressures were measured along the centerline of the crossing-shock interaction. Such measurements were made for each of the symmetric interaction cases described in Table 1. Results of these measurements showed good agreement with those obtained by the previous investigators.

The wall pressure measurements were also used to evaluate the upstream influence of the fin trailing edges. A series of wall pressure measurements was made for three different fin lengths in a $M_\infty = 3$, $\alpha_1 = \alpha_2 = 11°$ interaction. It was observed that the primary effect of increasing the fin length is to increase the peak pressure achieved on the interaction centerline. This is intuitive since, if the fins are long enough, the inviscid shocks will cross a second time and the wall pressure must continue to rise, "smoothing out" this crossing also. Results also showed that, within the accuracy of the measurements, there was no significant upstream propagation effect of fin length on the measured wall static pressure. Thus, it seems that the only effect of the fin length is to determine the downstream extent of the compression process.

Further details on the wall static pressure measurements and the influence of the model geometry can be found in References 11 and 18.

Skin Friction Measurements

As noted in Table 1, the skin friction measurements were made for three interactions, namely $M_\infty = 3$, $\alpha_1 = \alpha_2 = 7°$, $M_\infty = 3$, $\alpha_1 = \alpha_2 = 11°$, and $M_\infty = 3.85$, $\alpha_1 = \alpha_2 = 15°$. Relative to the overall test matrix, these three cases represent a weak, intermediate, and strong interaction, respectively. The measurements were made along the centerline of each interaction and along a spanwise cut from the interaction centerline to the fin surface.

Results for the $M_\infty = 3$, $\alpha_1 = \alpha_2 = 7°$ and $M_\infty = 3.85$, $\alpha_1 = \alpha_2 = 15°$ interactions are shown in Figures 7 and 8, respectively. For the weak interaction, Figure 7, the shear drops continuously along the interaction centerline but remains greater than zero everywhere. In contrast, the shear along the centerline of the strong interaction goes to zero, supporting the presence of the saddle point and boundary layer separation observed in the surface flow pattern for this interaction. For the spanwise distributions, both interactions show a strong peak C_f near the fin surface, corresponding to a line of flow attachment on the plate. For the strongest interaction, Figure 8, the peak C_f value is 5.5 times the flat plate skin friction value, $C_{f\infty}$.

The skin friction results obtained in the subject research program are unique data which provide valuable information on the crossing-shock interaction. They show that, in the stronger interactions, the wall shear goes to zero on the interaction centerline, supporting the presence of the saddle point and associated boundary layer separation observed in the surface flow patterns

and PLS visualizations. The measurements also show that, in addition to regions of very low shear, the crossing-shock interactions contain regions of extremely high shear. The presence and location of these high shear levels is consistent with that observed in previous single-fin studies.[25] Additionally, the skin friction data are extremely valuable for assessing CFD turbulence models used in predicting the crossing-shock flow.

A complete discussion of the C_f measurements is given in References 11 and 14.

5-Hole Probe Surveys

As noted earlier, the 5-hole probe surveys provide the local Mach number, M, pitot pressure, P_p, stagnation pressure, P_t, static pressure, P, and the pitch and yaw angles. Results obtained for the Mach number and static pressure distributions will be reviewed herein while details of the complete dataset can be found in References 11 and 16. For convenience, Reference 16 has been included as Appendix A.

Figure 9 shows the measured Mach number contours within the $M_\infty = 3.85$, $\alpha_1 = \alpha_2 = 15°$ interaction. The contours are for measurements made over an X-Y plane located at $Z/\delta_\infty = 32.3$ and correspond to the flowfield diagram shown as Figure 5L). In Figure 9, one can clearly see the large separated region on the interaction centerline which is comprised of low-Mach-number fluid.

Figure 10 shows the normalized static pressure contours, P/P_∞, at the same plane. Because the static pressure is sensitive even to weak waves, such contours reveal most of the flowfield features. Figure 11 shows the same static pressure contours with the corresponding flowfield diagram, Figure 5L), overlaid. From Figure 11, it can be seen that the static pressure contours compare quite well with the shock structure taken from the PLS images.

The complete dataset obtained through the five-hole probe surveys provides a valuable addition to the overall crossing-shock database. The contour plots not only complement the flowfield visualizations, but also serve to validate them. The survey results verify the existence of all the shock waves identified in the PLS images and provide information on their relative strengths. The survey data are also able to refine the exact locations of these waves. It was also shown that the separated region consists of a large, low-Mach-number, low-total-pressure region. Additional understanding of the flow behavior within this region was provided by the pitch and yaw contours, indicating the presence of a "mushroom"-shaped vortex pattern within the separated flow region, as depicted in Figure 5. Finally, the five-hole probe data provide an excellent dataset for comparison with computational solutions.

Asymmetric Interactions

As shown in Table 1, a limited set of experiments were made for asymmetric crossing-shock interactions in which $\alpha_1 \neq \alpha_2$. Because of the asymmetry, these interactions are more complex to analyze than symmetric cases. Based on the available data, it appears the primary effect of interaction asymmetry is to move the location of the separated region toward the weaker shock generator. Hence, one possible advantage of employing an asymmetric configuration is to shift the location of the separated flow region away from the interaction centerline. Further details on the structure of asymmetric crossing-shock interactions can be found in References 26-27. However, additional study is needed to completely characterize these flows.

Triple-Shock Interaction

A sequence of 9 PLS images of the triple-shock interaction is given in Figure 12. Analogous to the crossing-shock results described above, these images can be used to determine the location of the shock waves, sliplines, and separated flow regions within the interaction.

Figure 13 shows the flowfield model developed from the images of Figure 12. Because of the symmetry of the triple-shock interaction, only the right half of the flowfield is shown in Figure 13. Also shown in Figure 13 is a top view of the interaction illustrating the locations of the 9 PLS images relative to the model geometry.

To understand the triple-shock interaction, it proved useful to consider an equivalent reflection of a corner-flow interaction from a inviscid wall. The same approach proved extremely valuable in the analysis of the crossing-shock interaction described earlier in which the reflection of a single-fin interaction was used.

The triple-shock flowfield depicted in Figure 13 is very complex and will not be described in detail herein; a complete description is given in Reference 13, which is included as Appendix B. However, a very important conclusion can be made by comparing the triple-shock images of Figure 12 to crossing-shock images of Figure 3. Because the freestream Mach number and fin angles are the same for both cases, the only difference between these flows is the presence of the 10° compression ramp in the triple-shock configuration. Comparing the two flows shows that the separated flow region is significantly smaller in the triple-shock interaction, despite the fact that the overall compression is greater for this configuration. The size of the triple-shock separated region is approximately 45% smaller than that of the corresponding crossing-shock flow. This observation suggests that modifications to the crossing-shock geometry can be made to reduce the extent of the separated region and increase the overall inlet compression, hence producing a much more effective inlet configuration.

Comparison with Computational Solutions

In addition to providing valuable information on the physics governing the crossing-shock and triple-shock interactions, the experimental data described above provide an excellent dataset for CFD code validation. This section summarizes the results of comparisons made between the experimental data obtained in the subject research program with several computational solutions. While the computational solutions were performed by other investigators and are not part of the current research program, a significant amount of effort under this AFOSR grant was directed at interacting with the computationalists solving the crossing-shock and triple-shock flows. Much of this collaborative effort involved making detailed comparisons between the computational solutions and the experiments results obtained under this grant.

Data for the symmetric M_∞ = 3.85, $\alpha_1 = \alpha_2$ = 15° crossing-shock interaction has been compared to several computational solutions using Baldwin-Lomax and κ-ε turbulence models.[11,14,16,17,28,29] Also, computations using a κ-ε turbulence model have been compared to the triple-shock interaction,[13] and an asymmetric crossing-shock interaction.[26-27] While complete details of the comparisons can be found in the references, the following general conclusions can be made:

1.   Overall, the prediction of the skin friction coefficient by computations using κ-ε models was in best agreement with the experiment. However, all the turbulence models failed to accurately predict important aspects of the measured skin friction distribution. The errors

in the predicted skin friction distribution, along with errors in the computed surface flow patterns, suggest that improvements in the turbulence models are required.

2.   The largest errors in the computed flowfield occur within the separated flow region. Within this region, large errors are observed in the computed static pressure, flow angles, and Mach number. In addition to turbulence model problems, insufficient grid resolution and shock smearing are likely causes of the discrepancies.

3.   Outside of the separated region, where the flow is essentially inviscid, the computations are in better agreement with the experiment than inside it.

4.   While the skin friction comparison favors the κ-ε model, a comparison with the flowfield data shows that no turbulence model can be identified as being superior.

5.   The comparatively-low resolution in the computations makes it difficult to identify individual waves within the flowfield. Thus, it is extremely difficult to develop a detailed flowfield model based on the computations alone.

6.   All the computations did predict a quasi-two-dimensional separation on the interaction centerline and the subsequent formation of a large, separated region, as confirmed by the experiments.

V. CONCLUSIONS

Based on results from the experimental measurements, the structure of the crossing-shock and triple-shock interactions has been revealed for the first time. The following conclusions can be made concerning the crossing-shock interaction:

1.   The crossing-shock interaction represents the confluence of two quasiconical single-fin interactions, from which a complex, fully-3D, viscous/inviscid interaction develops.

2.   By treating the symmetry plane as an inviscid reflection plane and analyzing the reflection of a single fin interaction, the flowfield wave structure of the crossing-shock interaction is revealed. This reflection-plane analogy, developed to understand the crossing-shock interaction, can be used to understand a variety of symmetric shock/boundary layer interactions.

3.   Results of the reflection-plane analysis show that the shock structure is comprised of a complex, irregular reflection of the single fin interaction. The irregular reflection process results in the formation of additional shock segments (*ie* Mach stems) and sliplines. The resulting shock wave pattern is significantly different from that which would be predicted from inviscid theory.

4.   Limiting streamline visualizations show that, for strong interactions, the entire incoming boundary layer separates from the plate surface, while for weaker interactions, only a portion of the incoming boundary layer separates.

5.   The separated incoming boundary layer is shown to collect in a large, vortical flow region located on the interaction centerline. Surveys of the separated flow show that it is a low-

Mach-number, low-total-pressure region. Such a region may have significant implications in the design of high-speed inlets.

6. Within the separated region, both the PLS visualizations and the five-hole probe surveys show the flowfield consists of a "mushroom"-shaped separation cell.

7. The wall shear stress was successfully measured using a Laser Interferometer Skin Friction meter. The skin friction measurements show that, for cases with complete boundary layer separation, the shear stress goes to zero on the interaction centerline. In addition, the LISF measurements show that the crossing-shock interactions contain regions of extremely high shear associated with a line of flow attachment.

8. Results of the experimental measurements are used to form the first detailed flowfield model of the crossing-shock interaction. Additionally, the structure of the flowfield model is shown to be qualitatively similar over a broad range of interaction strengths.

9. The flowfield model shows that the interaction between the outer inviscid flow and the viscous boundary layer substantially alters the structure of the flowfield from that predicted from inviscid theory alone. The viscous effects are seen to extend a significant distance above the model surface. This means that a failure to include such effects in the design of high-speed inlets would result in significant errors.

10. A comparison with available hypersonic interaction measurements suggests that the structure of the hypersonic interactions is similar to that of the stronger supersonic interactions examine herein.

11. The primary effect of asymmetry appears to be a shifting of the separated region away from centerline and toward the weaker shock generator.

Regarding the triple-shock flow, the following overall conclusions and observations have been reached:

1. The triple-shock interaction represents the confluence of two conical corner flows, from which a complex, fully-3-D, viscous/inviscid interaction develops.

2. By treating the symmetry plane as an inviscid reflection plane and analyzing the reflection of a corner flow, the flowfield structure of the triple-shock interaction was revealed.

3. Results of the reflection-plane analysis show that the shock structure is comprised of a complex reflection, resulting in the formation and elimination of various waves. The level of complexity of the flowfield goes well beyond that of the single-fin and crossing-shock interactions.

4. While there is boundary layer separation on the ramp, the extent of the separated region is significantly smaller than that produced in a crossing-shock interaction without the compression ramp. This result is very important in the design of high-speed inlets. It shows that higher inlet compression does not necessarily lead to more serious boundary layer separation and, in fact, can be used to reduce the separation if properly applied.
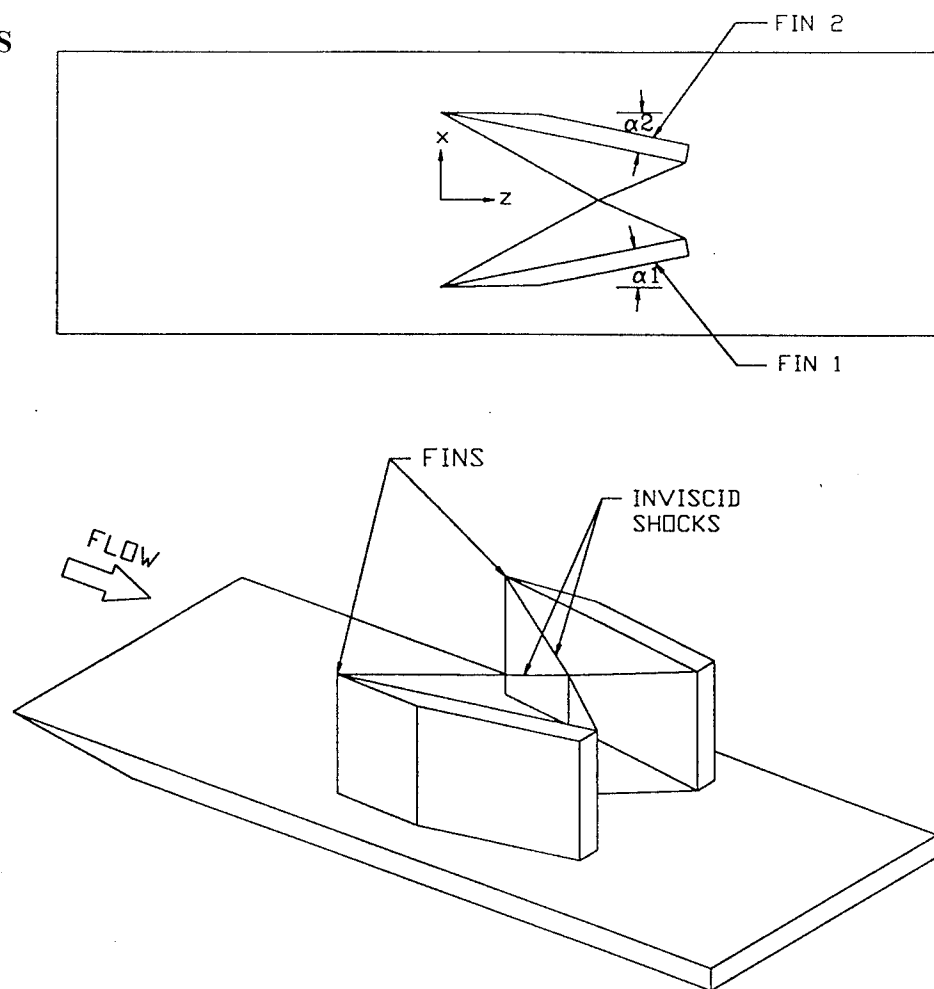
VI. FIGURES

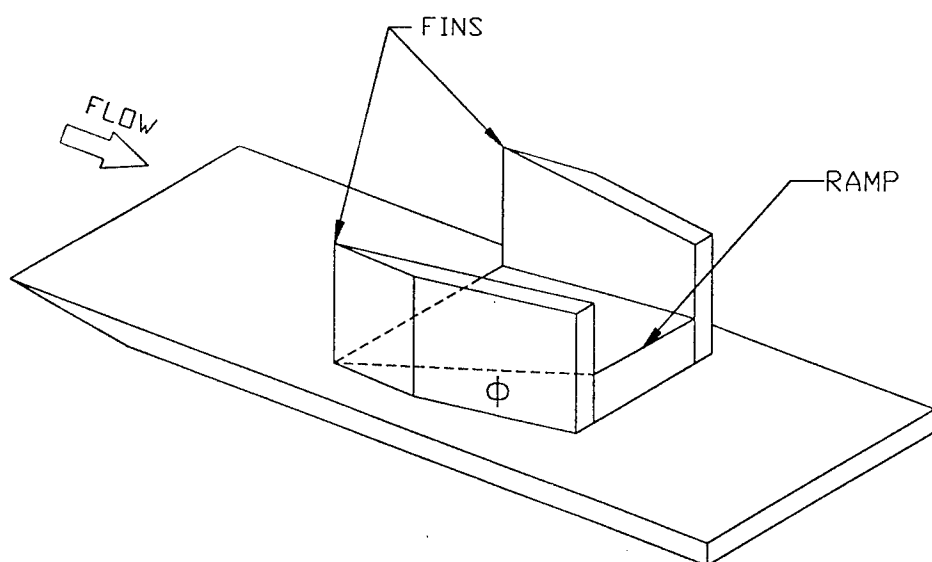**Figure 1** Top and perspective views of the crossing-shock test model.

Figure 2 Perspective view of the triple-shock test model.

(a)

(b)

(c)

(d)

(e)

(f)

(g)

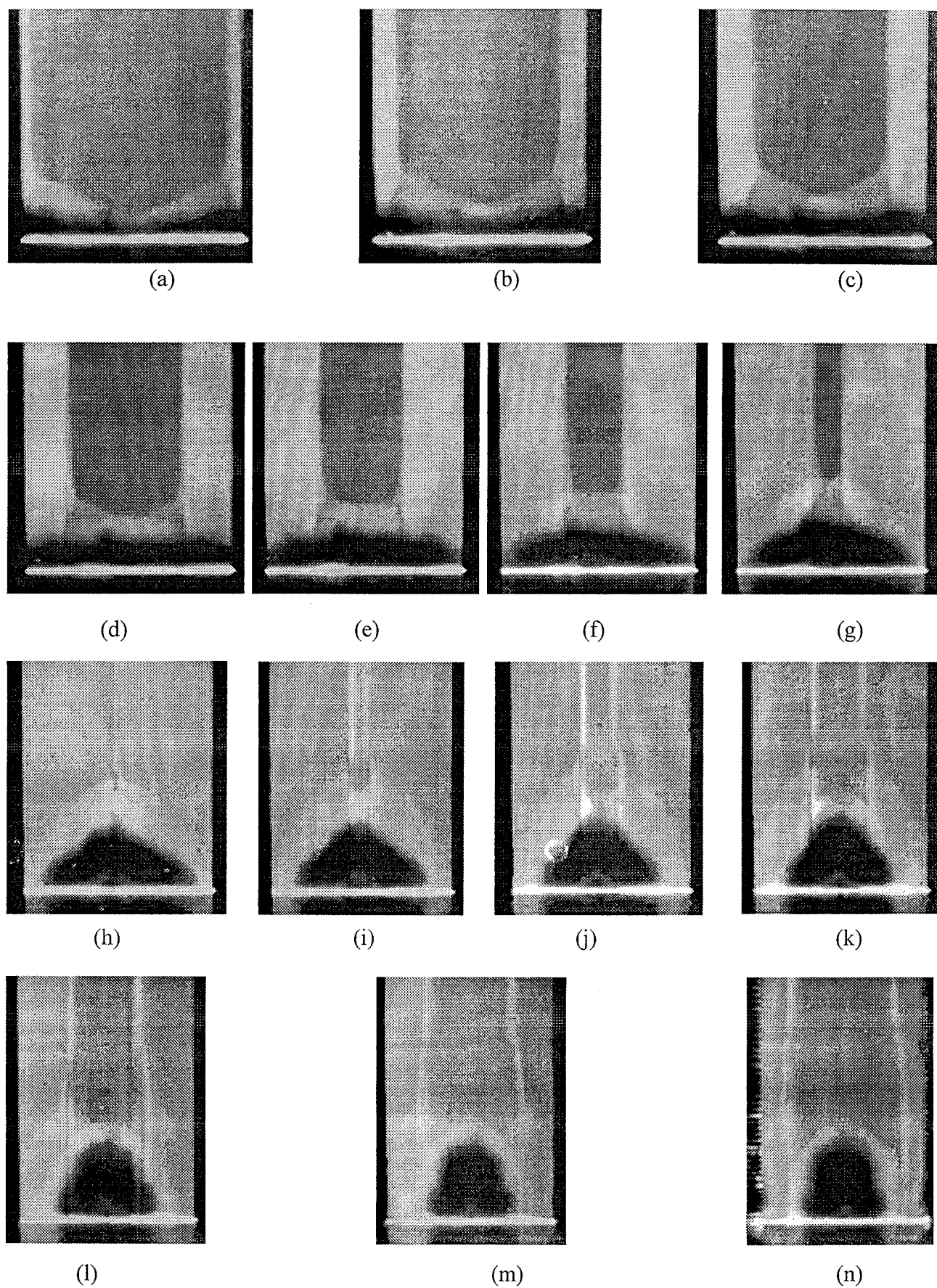(h)

(i)

(j)

(k)

(l)

(m)

(n)

Figure 3 PLS images for the $M_\infty = 3.85$, $\alpha_1 = \alpha_2 = 15°$ interaction.
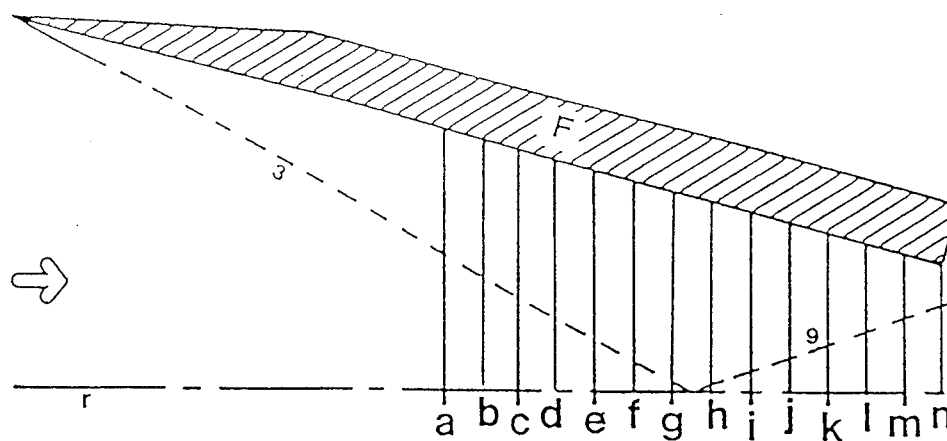
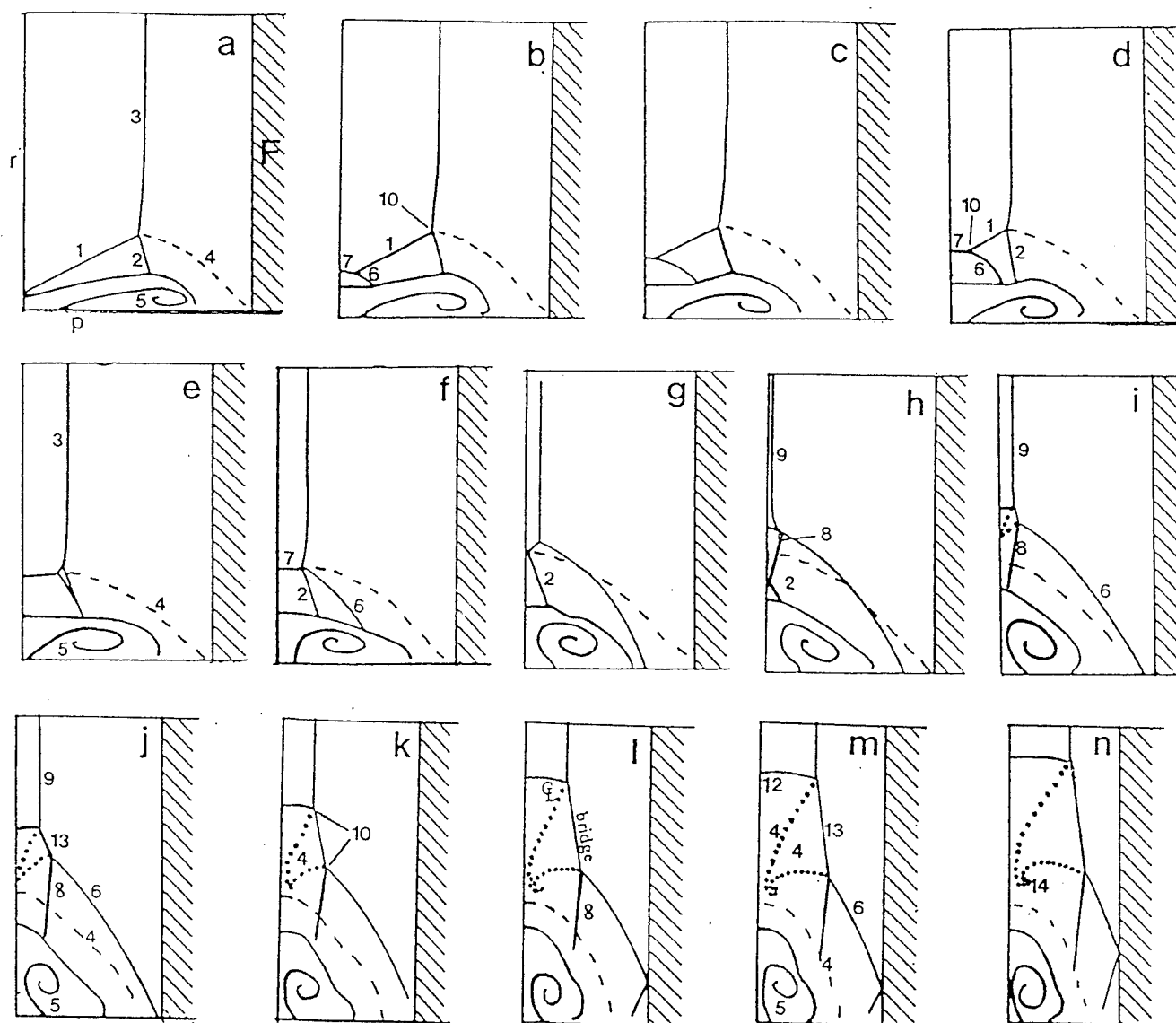**Figure 4** Locations of the PLS images shown in Figure 3.

Figure 5. Flowfield model for the Mach 3.85, $\alpha = 15°$ interaction. Key: F-fin, p-flat plate, r-reflection plane (model centerline), 1-incident separation shock, 2-incident rear shock, 3-incident "inviscid" shock, 4-slipline, 5-separation vortex, 6-reflected separation shock, 7-Mach stem, 8-reflected rear shock, 9-reflected "inviscid" shock, 10-triple point, 12-centerline shock, 13-bridge shock, 14-rolled up slipline.
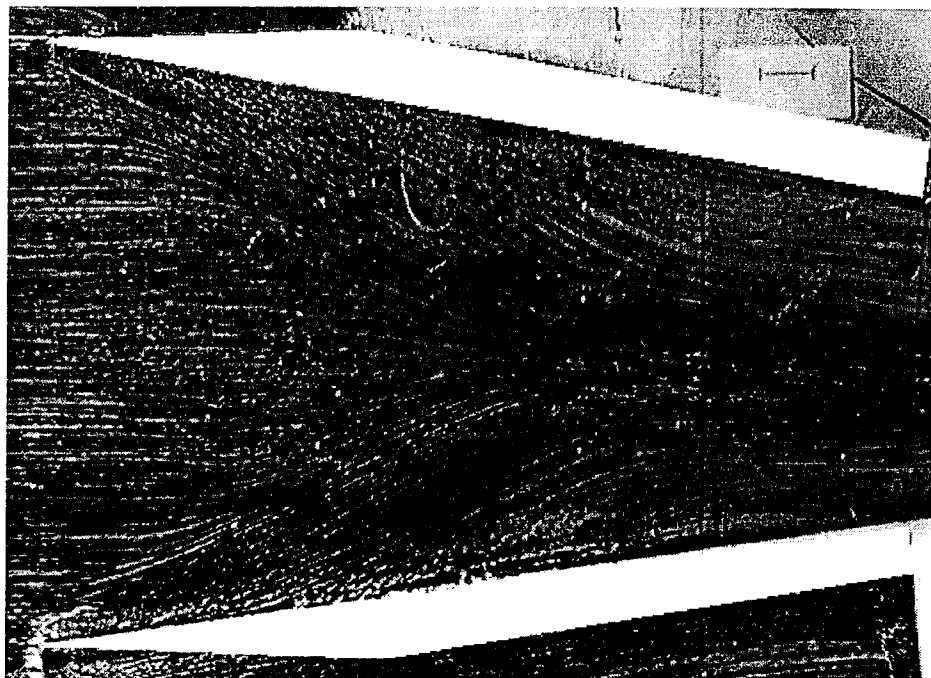
(a)
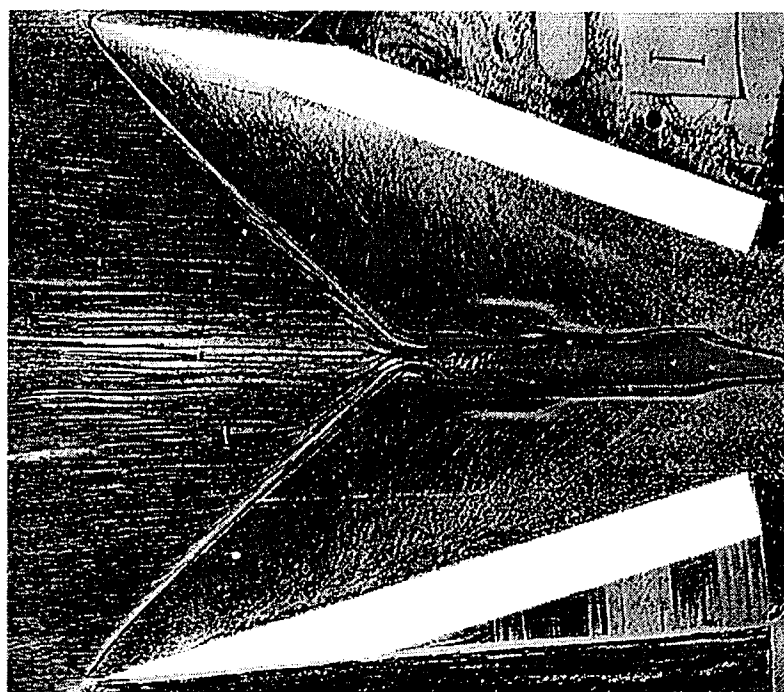
(b)

Figure 6 Surface flow patterns for a **(a)** $M_\infty = 3$, $\alpha_1 = \alpha_2 = 7°$ interaction and **(b)** $M_\infty = 3.85$, $\alpha_1 = \alpha_2 = 15°$ interaction
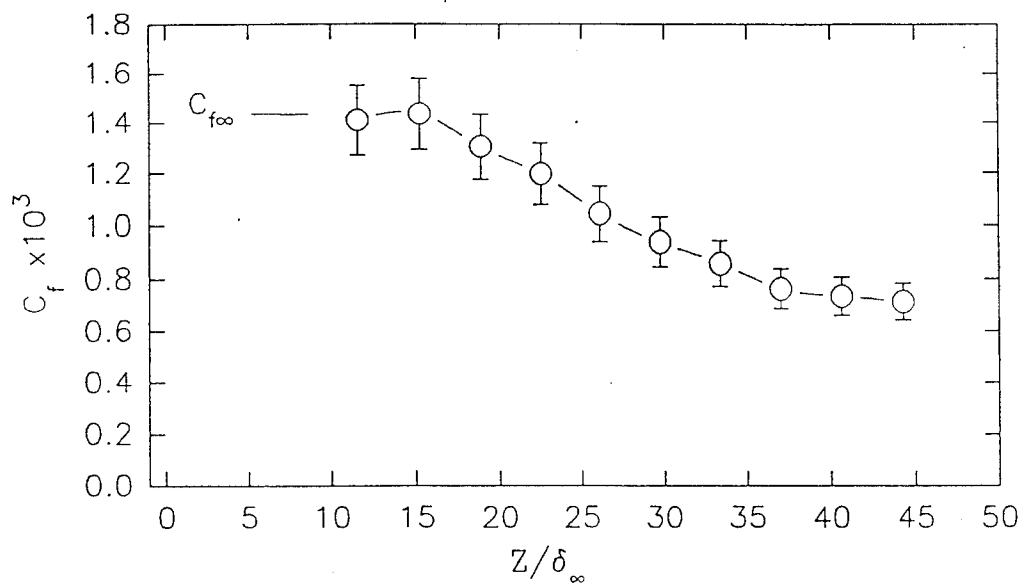
(a)
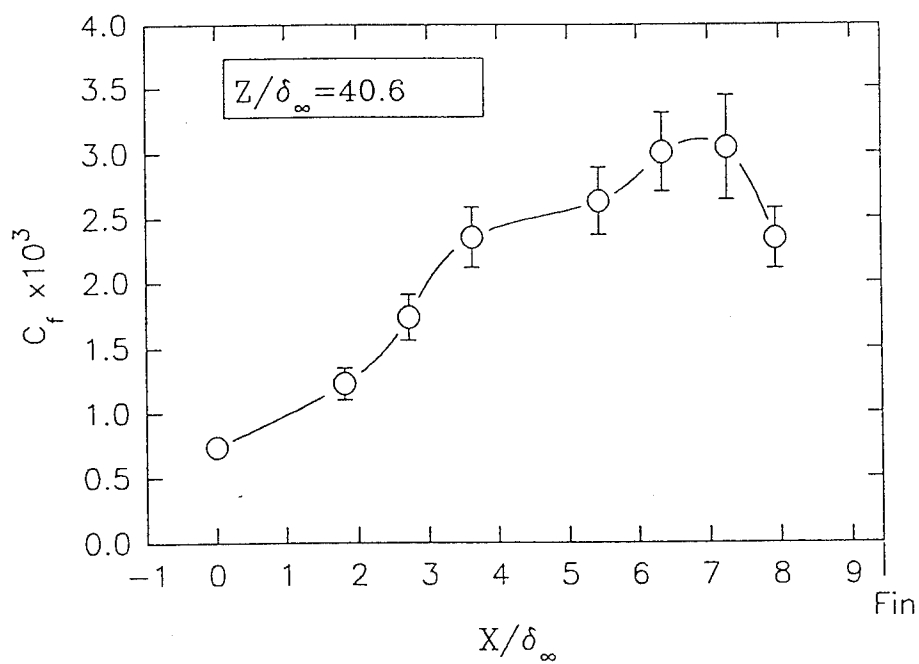
(b)

Figure 7 Skin friction coefficients for the $M_\infty = 3$, $\alpha_1 = \alpha_2 = 7°$ interaction: **(a)** C_f distribution along the interaction centerline and **(b)** C_f distribution along a spanwise cut at $Z/\delta_\infty = 40.6$.
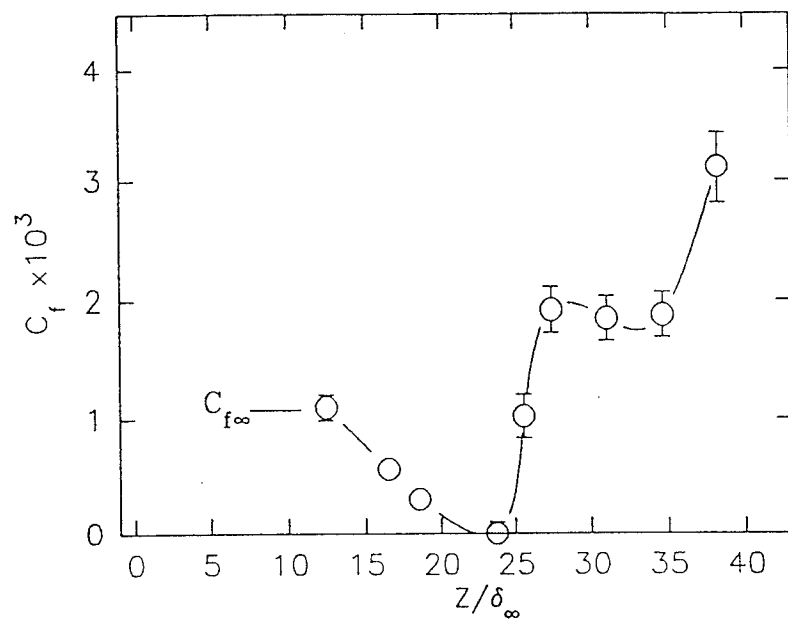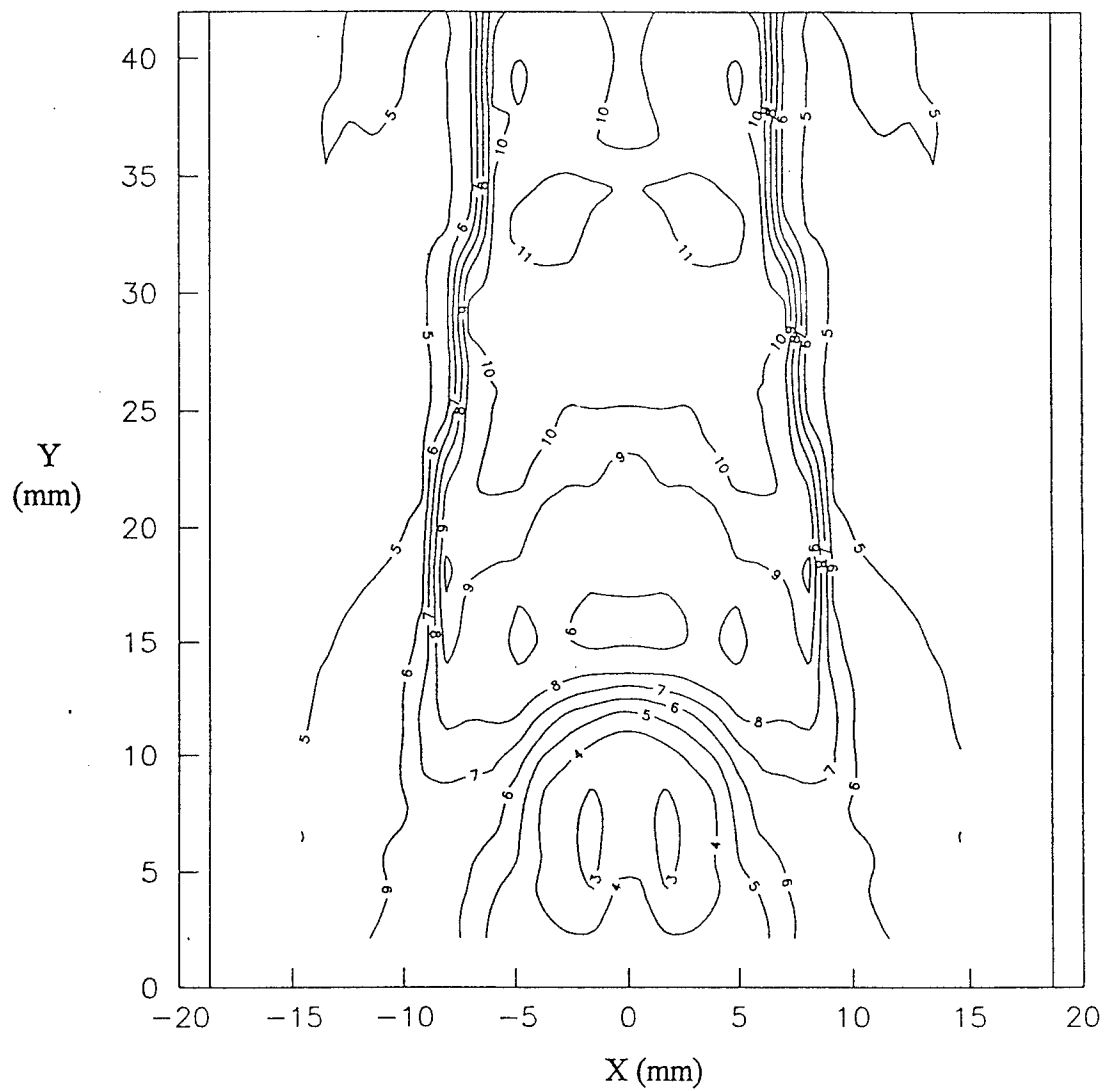
(a)
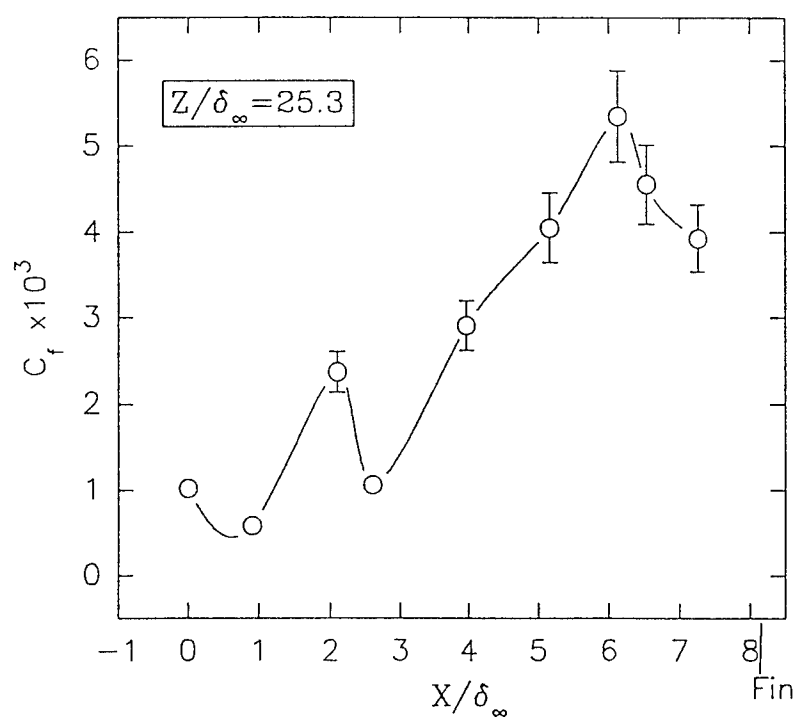
(b)

Figure 8 Skin friction coefficients for the $M_\infty = 3.85$, $\alpha_1 = \alpha_2 = 15°$ interaction: **(a)** C_f distribution along the interaction centerline and **(b)** C_f distribution along a spanwise cut at $Z/\delta_\infty = 25.3$.

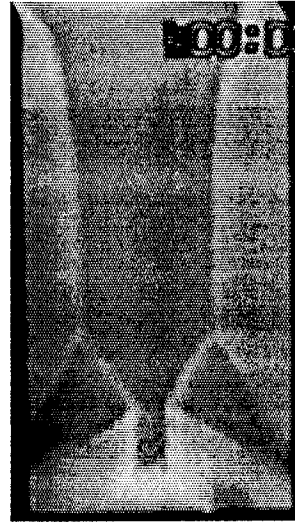**Figure 9** Mach number contours at $Z/\delta_\infty = 32.3$ corresponding to frame L of Figures 3 and 5.

Figure 10 Normalized static pressure contours, P/P_∞, at $Z/\delta_\infty = 32.3$ corresponding to frame L of Figures 3 and 5.
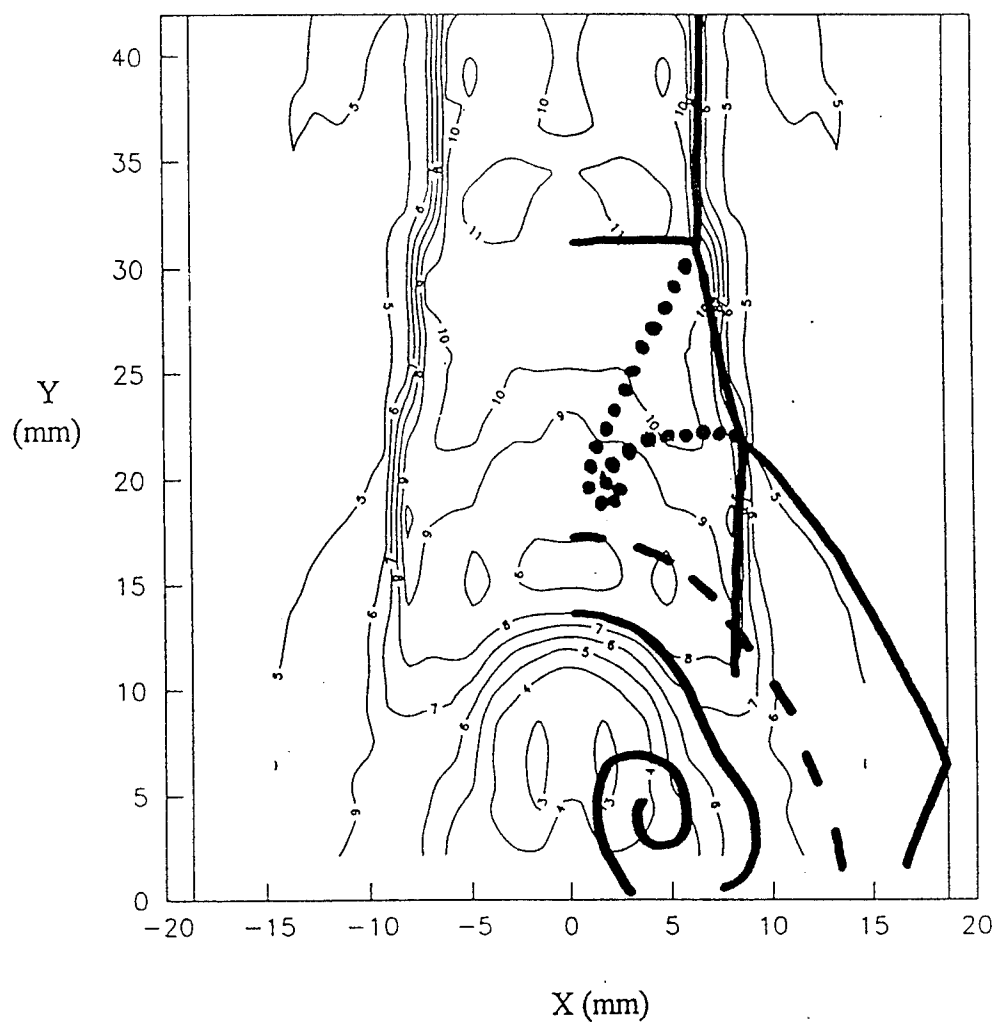
Figure 11 Comparison of the normalized static pressure contours with the PLS flowfield diagram at frame L of Figures 3 and 5.
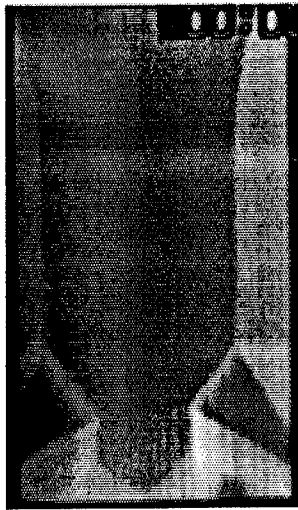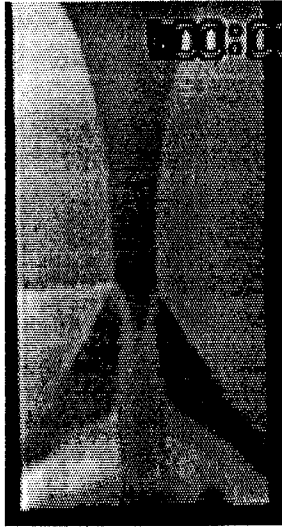
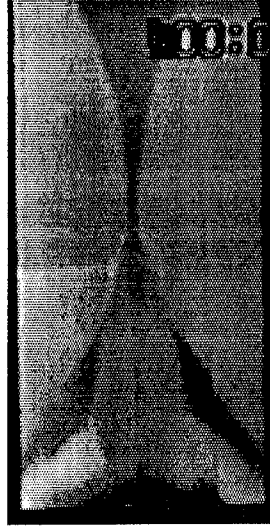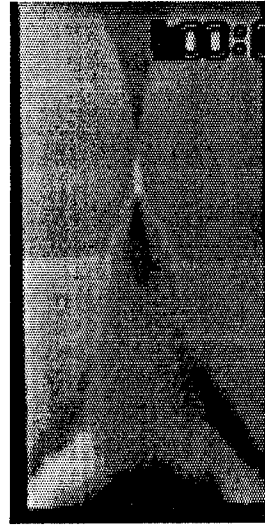a) $Z/\delta_\infty = 19.1$ b) $Z/\delta_\infty = 20.1$ c) $Z/\delta_\infty = 21.3$ d) $Z/\delta_\infty = 22.2$
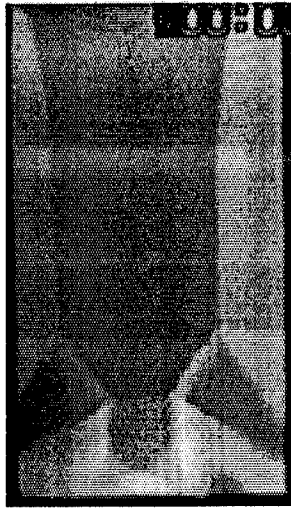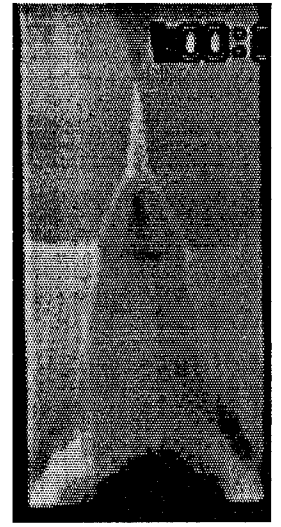
e) $Z/\delta_\infty = 24.2$ f) $Z/\delta_\infty = 25.7$ g) $Z/\delta_\infty = 26.7$ h) $Z/\delta_\infty = 27.7$

i) $Z/\delta_\infty = 29.3$ Figure 12 PLS images for a $M_\infty = 3.85$, $\alpha = 15°$, $\phi = 10°$ triple-shock interaction.

a) $Z/\delta_\infty = 19.1$ b) $Z/\delta_\infty = 20.1$ c) $Z/\delta_\infty = 21.3$ d) $Z/\delta_\infty = 22.2$

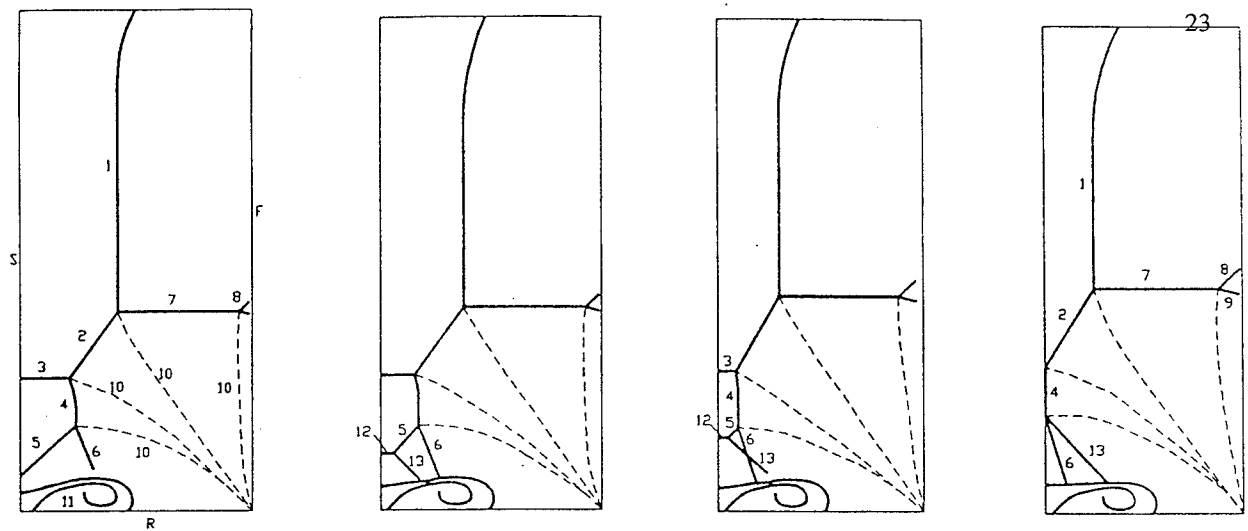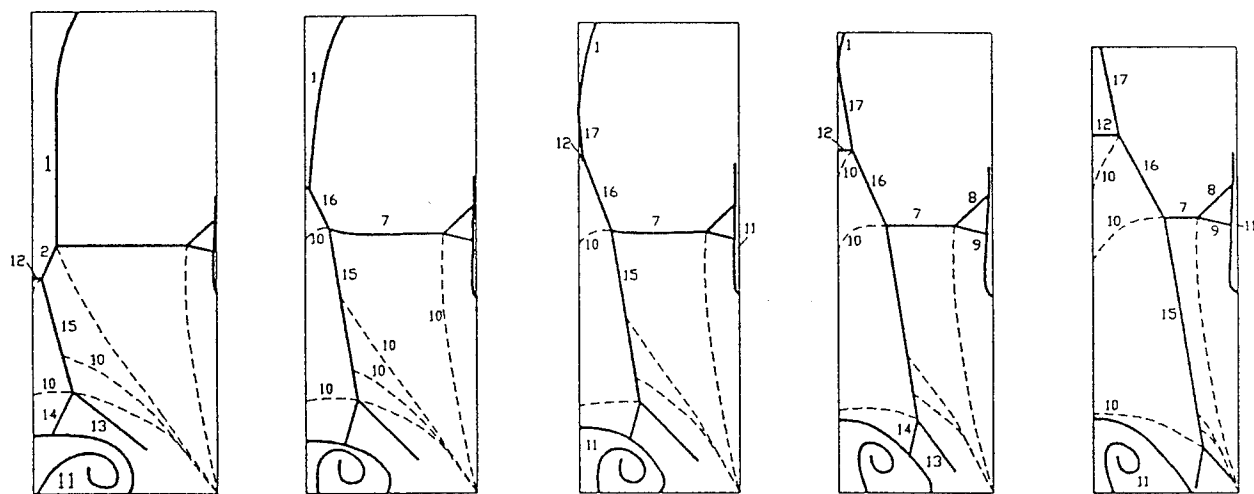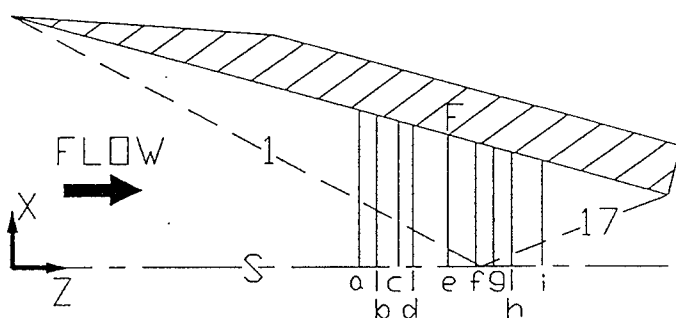e) $Z/\delta_\infty = 24.2$ f) $Z/\delta_\infty = 25.7$ g) $Z/\delta_\infty = 26.7$ h) $Z/\delta_\infty = 27.7$ i) $Z/\delta_\infty = 29.3$

Key: R - ramp
       F - fin
       S - symmetry (reflection) plane
       1 - fin inviscid shock
       2 - corner shock
       3 - ramp inviscid shock
       4 - fin embedded shock
       5 - fin separation shock
       6 - fin rear shock
       7 - ramp embedded shock
       8 - ramp separation shock
       9 - ramp rear shock
       10 - slipline
       11 - separated region
       12 - Mach stem
       13 - reflected fin separation shock
       14 - reflected fin rear shock
       15 - reflected corner shock
       16 - bridge shock
       17 - reflected fin inviscid shock

Figure 13 Flowfield diagrams for the $M_\infty = 3.85$, $\alpha_1 = \alpha_2 = 15°$, $\phi = 10°$ triple-shock interaction with top view showing the locations of each plane.

VII. PUBLICATIONS

The following is a list of publications which have resulted from the subject AFOSR grant.

1) Garrison, T.J. and Settles, G.S., "Flowfield Visualization of Crossing Shock-Wave/Boundary Layer Interactions," AIAA Paper 92-0750, Jan. 1992.

2) Garrison, T.J. and Settles, G.S., "Interaction Strength and Model Geometry Effects on the Structure of Crossing-Shock Wave/Turbulent Boundary-Layer Interactions," AIAA Paper 93-0780, Jan. 1993.

3) Garrison, T.J., Settles, G.S., Narayanswami, N., and Knight, D., "Structure of Crossing Shock-Wave/Turbulent Boundary Layer Interactions," *AIAA Journal*, vol.31, no. 12, Dec. 1993.

4) Garrison, T.J., Settles, G.S., Narayanswami, N., and Knight, D., "Laser Interferometer Skin-Friction Measurements of Crossing-Shock Wave/Turbulent Boundary-Layer Interactions," *AIAA Journal*, vol. 32, no. 6, June 1994.

5) Garrison, T.J., *The Interaction Between Crossing-Shock Waves and a Turbulent Boundary Layer*, Ph.D. Thesis, The Pennsylvania State University, M.E. Dept., August 1994.

6) Garrison, T.J., Settles, G.S., and Horstman, C.C., "Measurements and Computation of the Triple Shock Wave/Turbulent Boundary Layer Interaction," AIAA Paper 94-2274, June, 1994, submitted for publication in the *AIAA Journal.*

7) Garrison, T.J., Settles, G.S., Narayanswami, N., and Knight, D., Horstman, C.C., "Comparison of Flowfield Surveys and Computations of a Crossing-Shock Wave/Boundary Layer Interaction," AIAA Paper 94-2273, June, 1994, submitted for publication in the *AIAA Journal.*

8) Knight, D.D., Garrison, T.J., and Settles, G.S., "Investigation of Asymmetric Crossing Shock Wave-Turbulent Boundary Layer Interaction," in *Proceedings of the International Conference on Methods of Aerophysical Research*, Russian Academy of Sciences, Siberian Division, Novosibirsk, Russia, August 1994.

9) Knight, D.D., Garrison, T.J., Settles, G.S., Zheltovodov, A.A., Maksimov, A.I., Shevchenko, A.M., and Vorontsov, S.S., "Asymmetric Crossing Shock Wave-Turbulent Boundary Layer Interaction," accepted for presentation at AIAA 33rd Aerospace Sciences Meeting, Reno, NV, Jan. 1995.

VIII. REFERENCES

1. Mee, D.J., Stalker, R.J., and Stollery, J.L., "Glancing Interactions Between Single and Intersecting Oblique Shock Waves and a Turbulent Boundary Layer," *J. of Fluid Mechanics*, Vol. 170, 1986, pp. 411-433.

2. Batcho, P.F., Ketchum, A.C., Bogdonoff, S.M. and Fernando, E.M., "Preliminary Study of The Interactions Caused by Crossing Shock Waves and a Turbulent Boundary Layer," AIAA Paper 89-0359, Jan. 1989.

3. Bogdonoff, S.M., and Poddar, K., "An Exploratory Study of a Three-Dimensional Shock Wave Turbulent Boundary Layer Interaction in a Corner," AIAA Paper 91-0525, Jan. 1991.

4. Hingst, W.R., and Williams, K.E., "Interaction of Two Glancing, Crossing Shock Waves with Turbulent Boundary Layers at Various Mach Numbers," NASA TM 103740.

5. Bogdonoff, S.M., and Stokes, W.L., "Crossing Shock Wave Turbulent Boundary Layer Interactions -Variable Angle and Shock Generator Length Geometry Effects at Mach 3," AIAA Paper 92-0636, Jan. 1992.

6. Poddar, K. and Bogdonoff, S.M., "A Study of the Unsteadiness of Crossing Shock Wave Turbulent Boundary Layer Interactions," AIAA Paper 90-1456.

7. Narayanswami, N., Knight, D., Bogdonoff, S.M., and Horstman, C.C., "Interaction Between Crossing Oblique Shocks and a Turbulent Boundary Layer," *AIAA Journal*, vol.30, no. 8, Aug. 1992.

8. Reddy, D.R., "3-D Navier-Stokes Analysis of Crossing, Glancing Shocks/Turbulent Boundary Layer Interactions," AIAA Paper 91-1758, June 1991.

9. Gaitonde, D., and Knight, D.D., "Numerical Experiments on 3-D Shock Wave-Boundary Layer Interaction Generated by a Sharp Fin," AIAA Paper 88-0309, Jan. 1988.

10. Settles, G.S., and Teng, H.Y., "Flow Visualization Methods for Separated Three-Dimensional Shock Wave/Turbulent Boundary Layer Interactions," *AIAA Journal*, Vol.21, March 1983, pp. 390-397.

11. Garrison, T.J., *The Interaction Between Crossing-Shock Waves and a Turbulent Boundary Layer*, Ph.D. Thesis, The Pennsylvania State University, M.E. Dept., August 1994.

12. Garrison, T.J. and Settles, G.S., "Flowfield Visualization of Crossing Shock-Wave/Boundary Layer Interactions," AIAA Paper 92-0750, Jan. 1992.

13. Garrison, T.J., Settles, G.S., and Horstman, C.C., "Measurements and Computation of the Triple Shock Wave/Turbulent Boundary Layer Interaction," AIAA Paper 94-2274, June, 1994, submitted for publication in the *AIAA Journal*.

14. Garrison, T.J., Settles, G.S., Narayanswami, N., and Knight, D., "Laser Interferometer Skin-Friction Measurements of Crossing-Shock Wave/Turbulent Boundary-Layer Interactions," *AIAA Journal*, vol. 32, no. 6, June 1994.

15. Naughton, J., Cattafesta, L., and Settles, G., "A Miniature, Fast Response, 5-Hole Probe for Supersonic Flowfield Measurements", *AIAA Journal*, vol. 31, no. 3, Mar. 1993.

16. Garrison, T.J., Settles, G.S., Narayanswami, N., and Knight, D., Horstman, C.C., "Comparison of Flowfield Surveys and Computations of a Crossing-Shock Wave/Boundary Layer Interaction," AIAA Paper 94-2273, June, 1994, submitted for publication in the *AIAA Journal*.

17. Garrison, T.J., Settles, G.S., Narayanswami, N., and Knight, D., "Structure of Crossing Shock-Wave/Turbulent Boundary Layer Interactions," *AIAA Journal*, vol.31, no. 12, Dec. 1993.

18. Garrison, T.J. and Settles, G.S., "Interaction Strength and Model Geometry Effects on the Structure of Crossing-Shock Wave/Turbulent Boundary-Layer Interactions," AIAA Paper 93-0780, Jan. 1993.

19. Kussoy, M.I., and Horstman, K.C., "Intersecting Shock-Wave/Turbulent Boundary-Layer Interactions at Mach 8.3," NASA TM 103909, Feb. 1992.

20. Kussoy, M.I., Horstman, K.C., and Horstman, C.C., "Hypersonic Crossing Shock-Wave/Turbulent-Boundary-Layer Interactions," AIAA Paper 93-0781, Jan. 1993.

21. Kussoy, M.I. and Horstman, K.C., "Three-Dimensional Hypersonic Shock Wave/Turbulent Boundary-Layer Interactions," *AIAA Journal*, vol. 31, no. 1, Jan. 1993, pp. 8-9.

22. Narayanswami, N., Knight, D.D., and Horstman, C.C., "The Investigation of a Hypersonic 3-D Crossing Shock/Turbulent Boundary Layer Interaction," submitted to *Shock Waves*.

23. Narayanswami, N., Horstman, C.C., and Knight, D.D., "Numerical Simulation of Crossing Shock/Turbulent Boundary Layer Interaction at Mach 8.3 - Comparison of Zero- and Two-Equation Turbulence Models," AIAA Paper 93-0779, Jan. 1993.

24. Narayanswami, N., Horstman, C.C., and Knight, D.D., "Computation of Crossing Shock/Turbulent Boundary Layer Interactions at Mach 8.3," *AIAA Journal*, vol. 31, no. 8, Aug. 1993.

25. Kim, K.-S., Lee, Y., Alvi, F.S., and Settles, G.S., "Skin-Friction Measurements and Computational Comparison of Swept Shock/Boundary Layer Interactions," *AIAA Journal*, vol. 29, no. 10, Oct. 1991, pp. 1643-1650.

26. Knight, D.D., Garrison, T.J., and Settles, G.S., "Investigation of Asymmetric Crossing Shock Wave-Turbulent Boundary Layer Interaction," in *Proceedings of the International Conference on Methods of Aerophysical Research*, Russian Academy of Sciences, Siberian Division, Novosibirsk, Russia, August 1994.

27. Knight, D.D., Garrison, T.J., Settles, G.S., Zheltovodov, A.A., Maksimov, A.I., Shevchenko, A.M., and Vorontsov, S.S., "Asymmetric Crossing Shock Wave-Turbulent Boundary Layer Interaction," accepted for presentation at AIAA 33rd Aerospace Sciences Meeting, Reno, NV, Jan. 1995.

28. Gaitonde, D., and Shang, J.S., "Calculations on a Double-Fin Turbulent Interaction at High Speed," AIAA Paper 93-3432, Aug. 1993.

29. Gaitonde, D., and Shang, J.S., "The Structure of a Turbulent Double-Fin Interaction at Mach 4," AIAA Paper 94-2810, June 1994.

AIAA 94-2273

COMPARISON OF FLOWFIELD SURVEYS AND COMPUTATIONS OF A CROSSING-SHOCK WAVE/BOUNDARY LAYER INTERACTION

T.J. Garrison and G.S. Settles
Pennsylvania State University, University Park, PA

N. Narayanswami and D.D. Knight
Rutgers University, Piscataway, NJ

C.C. Horstman
NASA-Ames Research Center, Moffett Field, CA

25th AIAA Fluid Dynamics Conference
June 20-23, 1994 / Colorado Springs, CO

COMPARISON OF FLOWFIELD SURVEYS AND COMPUTATIONS OF A CROSSING-SHOCK WAVE/BOUNDARY LAYER INTERACTION

T.J. Garrison[*] and G.S. Settles[**]
Dept. of Mechanical Engineering, Pennsylvania State University
N. Narayanswami[†] and D.D. Knight[††]
Mechanical and Aerospace Engineering Dept., Rutgers University
C.C. Horstman[‡]
NASA-Ames Research Center

ABSTRACT

A joint experimental and computational study has been performed to investigate the flowfield structure created by two crossing oblique shock waves interacting with a turbulent boundary layer. Such an interaction is of practical importance in the design of high-speed sidewall-compression inlets. The interaction is created by a test model consisting of two sharp fins mounted at 15 degrees angle-of-attack to a flat plate, placed in a Mach 3.85 freestream flow. Two computational solutions, one using a Baldwin-Lomax algebraic turbulent eddy viscosity model and one using a modified κ-ε (Rodi) turbulence model, are compared with experimental flowfield data obtained from a fast-response five-hole probe. Both the experiment and the computations show that the flowfield is dominated by a large, low-Mach-number, low-total-pressure separated region located on the interaction centerline. A comparison of the results shows significant differences between experiment and computations within this separated region. Outside the separated region, the experiment and computations are in good agreement. Additionally, the comparison shows that both turbulence models provide similar results, with neither model being clearly superior in predicting the flowfield.

INTRODUCTION

Shock wave boundary layer interactions can arise in a variety of situations associated with high-speed flight vehicles. For example, such interactions occur at control surfaces, wing/fuselage junctions, and within many components of the propulsion system. One particular area of current interest is associated with the interactions created in a high-speed inlet. Within the inlet, the flowfield properties are strongly influenced by the nature of the shock wave boundary layer interactions which occur therein. Such interactions can produce complex shock wave patterns and large-scale flow separation, both of which significantly alter the inlet flow and subsequently affect the overall engine performance. Additionally, the large drag and heat transfer rates as well as fatigue loads due to interaction unsteadiness impose structural constraints on the inlet. Thus, an understanding of the shock wave/boundary layer interactions within such inlets is paramount for effective inlet design.

One particular inlet configuration which has received a great deal of research attention in recent years is shown in Fig. 1a). This configuration simulates a generic high-speed sidewall-compression inlet, within which a pair of crossing oblique shock waves interacts with an incoming boundary layer. The flowfield created by this configuration, termed a crossing-shock interaction, has been studied both experimentally and computationally for a range of supersonic and hypersonic interactions. The majority of the experimental studies have focused on measurements made on the model surface,[1-7] with only a limited amount of data being available within the outer flowfield.[8-14] The data from these experiments have been used to understand the crossing-shock flow and to assess several computed solutions of the flowfield.[15-21] While these experimental and computational efforts have shed a great deal of light on the structure of the crossing-shock interaction, the lack of experimental flowfield data has restricted the understanding of the outer flow as well as limited the evaluation of the computed solutions.

To address the need for additional flowfield data, five-hole probe measurements were recently made for a strong, supersonic crossing-shock interaction. The goals of this paper are to describe the results of those measurements and to compare the experimental data with two computational solutions using different turbulence models. The results provide significant additional insight into the interaction physics as well as highlight the capabilities of current CFD models to predict a complex flow such as the crossing-shock interaction.

[*]Graduate Research Assistant, Student Member AIAA.

[**]Professor of Mechanical Engineering and Director, Gas Dynamics Laboratory, Associate Fellow AIAA.

[†]Research Staff; currently Research Associate, Institute of Fluid Science, Tohoku University, Sendai, Japan, Member AIAA.

[††]Professor of Mechanical and Aerospace Engineering, Associate Fellow AIAA.

[‡]Senior Scientist, Associate Fellow AIAA.

identify the various features shown in Fig. 2 is consistent with that of Ref. 9.

The main features of interest within the flowfield model are the large separated flow region on the interaction centerline and the complex overlying shock structure. Within the separated region, two counter-rotating vortices are known to reside, with the approximate configuration of the vortex to the right of the symmetry plane identified in Fig. 2. The intent of the remaining discussion is to supplement this semi-quantitative model with the detailed five-hole probe data and to compare the results with the two computed solutions. For more detailed information on the complete flowfield model the interested reader should consult Refs. 9 and 14.

Static Pressure

Fig. 3 shows the normalized static pressure contours, P/P_∞, obtained from the experimental five-hole probe surveys. Because the static pressure is sensitive even to weak oblique waves, such contours reveal most of the flowfield features. Fig. 4 shows the same static pressure contours with the corresponding flowfield diagram extracted from the PLS visualizations (Fig. 2) overlaid. From Fig. 4, it can be seen that the static pressure contours compare quite well with the shock structure taken from the PLS images. In this figure, the reflected separation, rear, and inviscid shocks, along with the "bridge" shock, are easily identified. The shock segment labeled the "centerline shock" in Fig. 2 does not clearly appear in the experimental pressure contours of Fig. 4, but can be verified by plotting the static pressure along discrete vertical cuts. The sliplines are not expected to appear, since they are streamlines across which a static pressure jump cannot occur.

In addition to locating shock waves, the static pressure contours can be used to gauge the strength of the various waves. From Fig. 4, it can be seen that the reflected separation shock is relatively weak, inducing only a slight static pressure rise. In contrast, the reflected rear shock is much stronger, with a pressure rise across it comparable to that across the reflected inviscid shock. Similarly, the bridge shock is comparable in strength to the reflected inviscid shock, while the centerline shock is very weak.

Figs. 5 and 6 provide a comparison between the experimental normalized static pressure contours and those predicted by the B-L and κ-ε computations, respectively. In these figures, data for $X > 0$ are experimental while data for $X < 0$ are computational. (Effectively, the experimental data to the left of the centerplane in Fig. 3 has been removed and replaced with the computational results.) It is possible to compare the results in this manner because of the symmetry of the crossing-shock interaction. It should also be noted that the contour increment is the same for both experiment and computation.

There are several important observations that can be made from Fig. 5 and 6. Considering the separated flow region first, there are significant differences between the computations and experiment within this region. The experimental contours show that the static pressure decreases significantly toward the center of this region while the computations predict a nearly uniform static pressure distribution. Additionally, in the experiment, the static pressure contours clearly delineate the size and shape of the separated region, but its presence is indiscernible in both computations. However, as shown in the following section, the separated region *is* apparent in the computed pitot pressure. Thus, the separated region is present in the computations but just not revealed by the static pressure. This is discussed further in the following section.

It is also clear from these figures that the computations are unable to precisely capture the shock waves within the flowfield. Even the pressure rise of the reflected inviscid shock, a strong wave which is unaffected by the underlying viscous effects, is spread over a significant distance. This is especially true for the κ-ε computation. The smearing of the shock waves by the computations is significantly greater than that by the 5-hole probe, and is orders of magnitude greater than that of the PLS images shown Refs. 8, 9 and 14. Referring to Fig. 2, a majority of the waves within the interaction, such as the reflected separation and rear shocks and the bridge shock, cannot easily be distinguished as separate, distinct waves within the computations.

The contour plots shown in Figs. 5 and 6 provide a means to compare data over the entire plane. However, from these plots it is somewhat difficult to quantitatively assess the degree to which the experiment and computations differ. For this purpose, it is more useful to compare the experiment and computations along discrete lines or "cuts". This is done in Fig. 7, which shows the static pressure variation in the Y direction at two X locations, namely $X = 0$ and $X = \pm 5$ mm. Fig. 7a) shows the normalized static pressure variation along the symmetry plane ($X = 0$). From this figure, it is clear that within the separated region ($Y < \approx 12$ mm) the computations significantly overpredict the static pressure by as much as factor of 2.5. Above the separated region, where the flow is essentially inviscid, the computations and experiment are in good agreement. Overall, the pressure variation along the symmetry plane predicted by the B-L model is in slightly better agreement with the experiment than that predicted by the κ-ε model.

Along the cut at $X = \pm 5$ mm, Fig. 7b), which passes along the outside edge of the separated region, similar conclusions can be drawn. However, the errors near $Y = 0$ are not as large as those in Fig. 7a). Comparing Figs. 5-7, it can be seen that the computational results are similar and that neither computation can be identified as being superior.

Pitot Pressure

Fig. 8 shows the experimental normalized pitot pressure contours, $P_p/P_{t\infty}$, and Figs. 9 and 10 compare these experimental contours to those predicted by the B-L and κ-

3

contours clearly show the reflected inviscid shocks, across which there are large yaw angle variations. Between the reflected inviscid shock and the fin, the yaw angle is 15°, while in the region between the reflected inviscid shocks, the yaw angle is zero. This is as predicted from inviscid theory and are required to satisfy continuity. The yaw angles also show the reflected separation and rear shocks as well as the bridge shock. The centerline shock does not appear, since it is horizontally-oriented.

It should be noted that the contouring routine used here produces an anomaly in the yaw contours in which non-zero contour lines cross the centerplane. Clearly, the symmetry of the crossing-shock interaction requires that the yaw angle be zero everywhere on the plane of symmetry. However, on either side of the centerplane, the yaw angles may be non-zero. In instances were non-zero yaw angles occur close to the centerline the contour package erroneously connects these points across the centerline. Thus, this artifact must be ignored in interpreting the resulting contours.

Inside the separated region, near the plate surface, the yaw angles are negative, indicating that the flow is being directed toward the centerplane. Near the top of the separated region, in the vicinity of the centerplane, the flow is directed away from the centerplane. However, at the top of the separated region and slightly further from the centerplane, the yaw angle becomes negative and the flow is once again directed toward the centerline.

By combining these observations with the previously described pitch angle results, the flowfield structure within the separated region can be determined. This is done in Fig. 17. The result is the "mushroom-shaped" vortical pattern shown previously in the schematic of Fig. 2.

Fig. 18 compares the computed and experimental pitch angles, ϕ, for cuts at X = 0 and ± 5 mm. Along the plane of symmetry, the peak pitch angle within the separated region is accurately predicted by the κ-ε computation and under-predicted by the B-L computation. However, both computations underpredict the vertical extent of the high-pitch region within the separated flow. In the outer flow, both computations match the experimental data.

For the cut along the line X = ± 5 mm, Fig. 18b), the comparison between the experiment and computations is not as good. Within the separated region, both computations significantly underpredict the extent to which the flow is directed downward, toward the plate. This indicates that the computations are most likely not capturing the full details of the "mushroom-shaped" vortex pattern within the separated region, as shown in Fig. 17. Above the separated region, the computations again accurately represent the experimental data.

The computed yaw angles, Ψ, are compared to the experiment in Fig. 18. Because of the symmetry of the crossing-shock interaction, the yaw angle must be zero everywhere along the line X = 0. Thus, comparing the results along this cut yields nothing interesting. Instead, Fig. 18 compares the data along cuts at X = ± 1 and ± 5 mm.

In both cuts, the computations differ significantly from the experiments over the range from Y = 5 to 10 mm, with Ψ differences up to 10° in this region. Over the rest of the region, the computations are within 2° of the experimental results. As with the pitch results, the large errors in yaw angle within the separated region suggest that the computations are not completely capturing the flow pattern in this area.

FURTHER COMMENTS ON THE COMPARISON

Based on the comparison of the flowfield data with the computed solutions presented in the previous sections, several important conclusions can be made. Within the separated region, distinct differences are apparent between the experiment and computations. From the point of view of understanding the interaction between the outer inviscid flow and the viscous boundary layer, the separated region represents the most important aspect of the crossing-shock interaction. Globally, both computations are able to predict the presence of this region. However, there are significant differences in the values of the flowfield properties predicted within the region. This suggests the computations are not fully capturing all the physics which govern the interaction.

It is important to understand possible reasons why the computations are in error within the separated region. One likely source of error is in the turbulence models employed. The fluid within the separated region has been shown to be comprised of the incoming viscous turbulent boundary layer. Thus, one would expect that the properties in this region would be dependent on the turbulence model. Additionally, it was seen in a previous comparison of the wall skin friction distribution[7] that large errors in the computed wall shear stress occur along the interaction centerline, supporting the argument that the turbulence modeling is in error in this region. Here, both B-L and κ-ε turbulence models fail in regions of strong gradients, as in 2-D compression corner flows with significant separation.

A second possible source of error lies in the resolution of the computations. It was seen in the previous discussions that the computations smear shock waves, making it difficult to identify discrete waves. To capture the effects of the plate and fin boundary layers, the computations must have sufficient grid resolution near the model surfaces. However, memory and CPU time constraints then require that the grid resolution must become much coarser away from the surface. The coarse outer grid makes it difficult to precisely capture shocks, resulting in a "smearing" of the shock waves over a significant distance. This can have a significant impact on the predicted flow directions and property values, especially the static pressure.

[17]Narayanswami, N., Knight, D., Bogdonoff, S.M., and Horstman, C.C., "Interaction Between Crossing Oblique Shocks and a Turbulent Boundary Layer," *AIAA Journal*, vol.30, no. 8, Aug. 1992.

[18]Narayanswami, N., Knight, D.D., and Horstman, C.C., "The Investigation of a Hypersonic 3-D Crossing Shock/Turbulent Boundary Layer Interaction," *Shock Waves*, Vol. 3, No. 1, 1993.

[19]Narayanswami, N., Horstman, C.C., and Knight, D.D., "Numerical Simulation of Crossing Shock/Turbulent Boundary Layer Interaction at Mach 8.3 - Comparison of Zero- and Two-Equation Turbulence Models," AIAA Paper 93-0779, Jan. 1993.

[20]Narayanswami, N., Horstman, C.C., and Knight, D.D., "Computation of Crossing Shock/Turbulent Boundary Layer Interactions at Mach 8.3," *AIAA Journal*, vol. 31, no. 8, Aug. 1993.

[21]Gaitonde, D., and Shang, J.S., "Calculations on a Double-Fin Turbulent Interaction at High Speed," AIAA Paper 93-3432, Aug. 1993.

[22]Naughton, J., Cattafesta, L., and Settles, G., "A Miniature, Fast Response, 5-Hole Probe for Supersonic Flowfield Measurements", *AIAA Journal*, vol. 31, no. 3, Mar. 1993.

[23]Naughton, J.W., *The Enhancement of Compressible Turbulent Mixing Via Streamwise Vorticity*, Ph.D. Thesis, The Pennsylvania State University, M.E. Dept., May 1993.

[24]Rubesin, M. and Rose, W., "The Turbulent Mean Flow Reynolds-Stress and Heat Flux Equations in Mass Averaged Dependent Variables," NASA TMX 62248, 1973.

[25]Baldwin, B. and Lomax, H., "Thin Layer Approximation and Algebraic Model for Separated Turbulent Flows," AIAA Paper 78-257, Jan. 1978.

[26]Knight, D., "A Hybrid Explicit-Implicit Numerical Algorithm for the Three Dimensional Compressible Navier-Stokes Equations," *AIAA Journal*, Vol. 22, No. 8, 1984, pp. 1056-1061.

[27]Rodi, W., "Experience with Two-Layer Models Combining the κ-ε with a One-Equation Model Near the Wall," AIAA Paper No. 91-0216, Jan. 1991.

[28]MacCormack, R.W., "A Numerical Method for Solving the Equations of Compressible Viscous Flow", AIAA Journal, Vol. 20, no. 9, Sept. 1982.
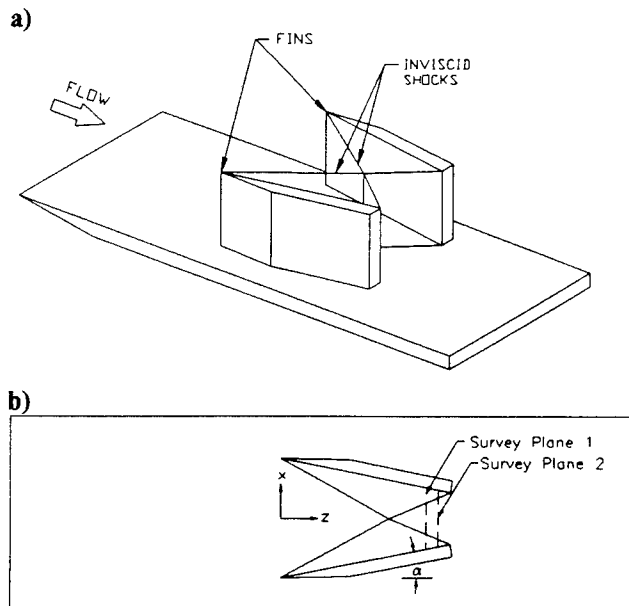
a)

b)

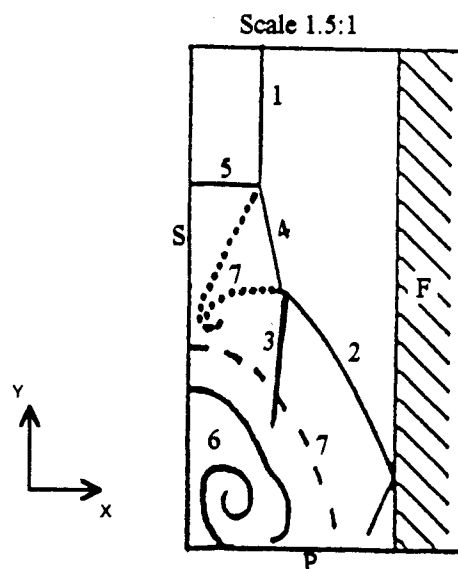**Figure 1 Experimental crossing-shock model a) perspective view, b)top view.**

Figure 2 Flowfield model at Z = 113 mm. Key: P - plate, F - fin, S - symmetry plane, 1 - reflected inviscid shock, 2 -reflected separation shock, 3 - reflected rear shock, 4 - bridge shock, 5 - centerline shock, 6 - separated flow region, 7 - sliplines.
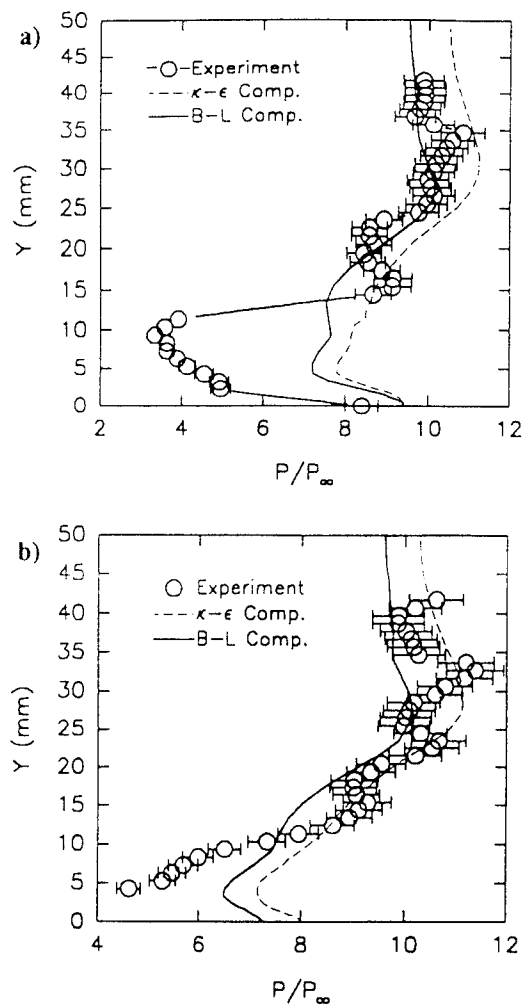
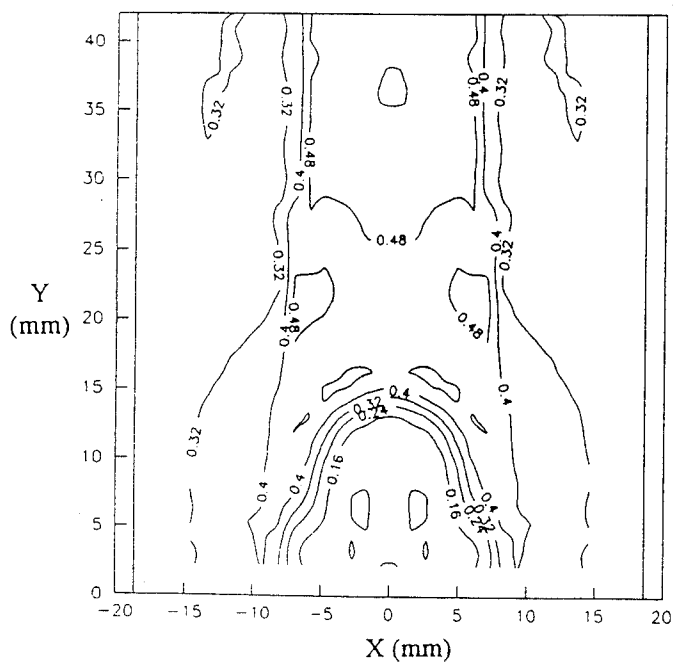Figure 7 Comparison of static pressure variation in the Y direction at a) X = 0 mm and b) X = ± 5 mm.

Figure 8 Experimental pitot pressure contours, $P_p/P_{t\infty}$.
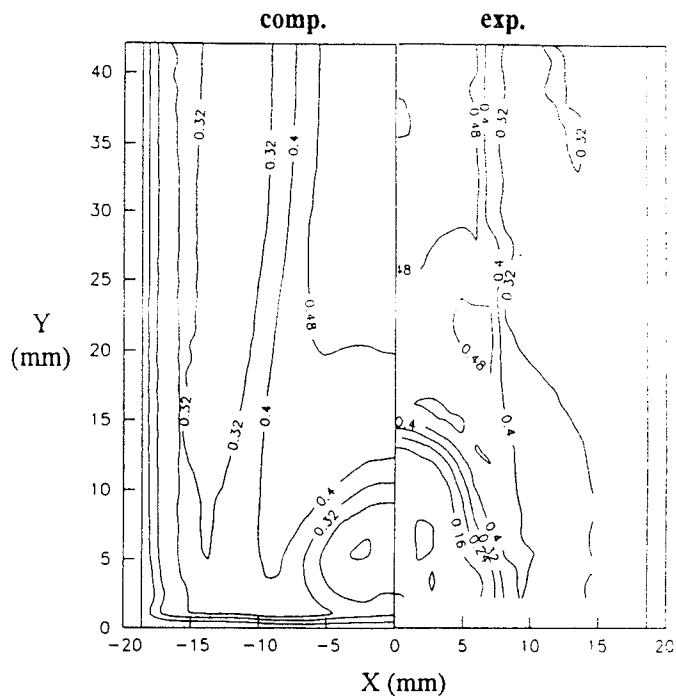

Figure 9 Comparison of the pitot pressure, $P_p/P_{t\infty}$, predicted by the B-L computation.
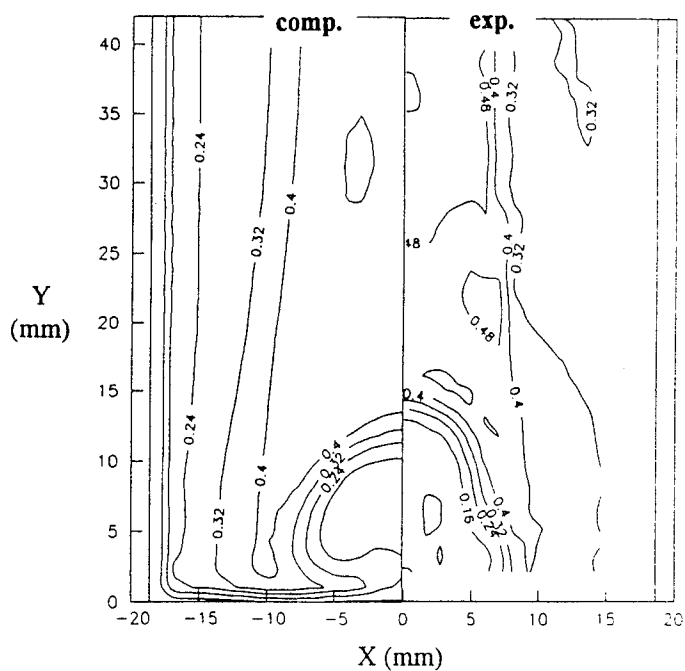

Figure 10 Comparison of the pitot pressure, $P_p/P_{t\infty}$, predicted by the κ-ε computation.

9

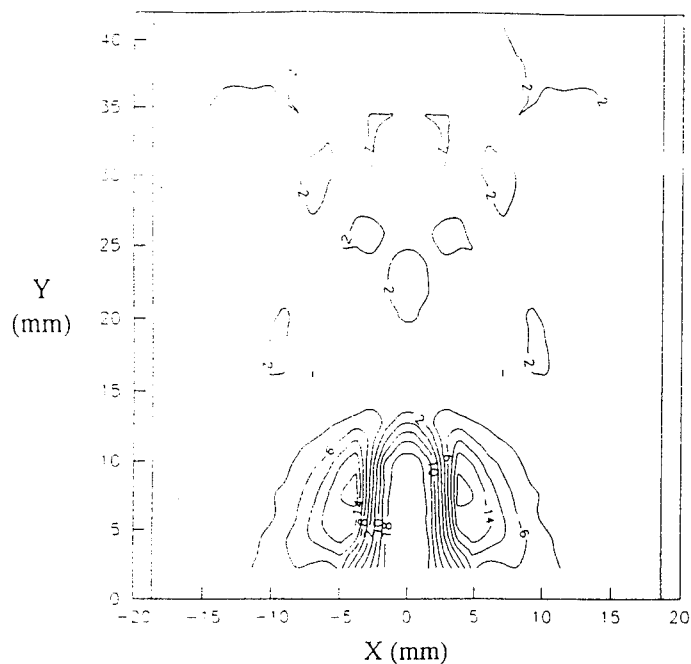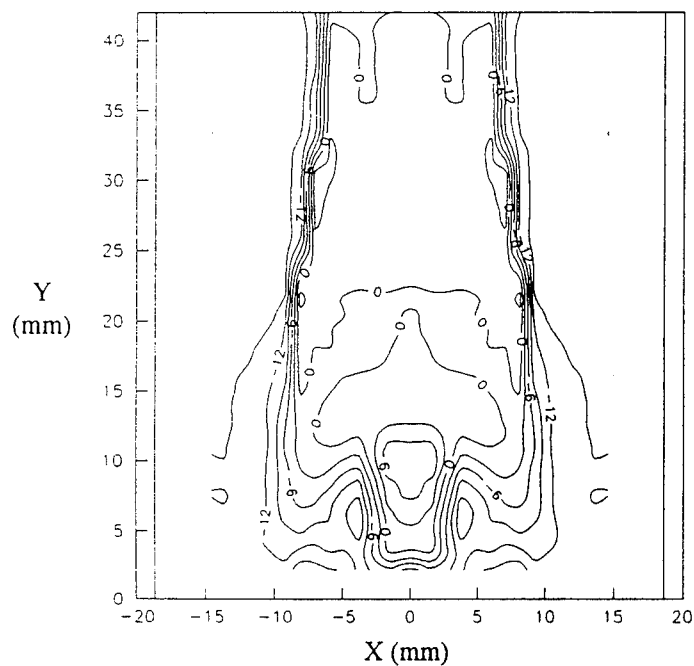**Figure 15 Experimental pitch angle contours.**
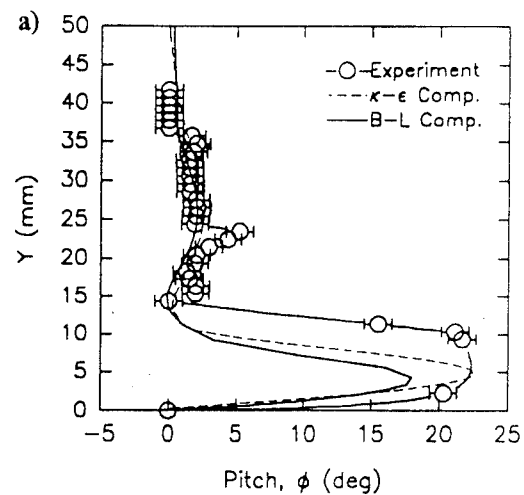

Figure 17 Flow pattern within the separated region.

Figure 16 Experimental yaw angle contours.
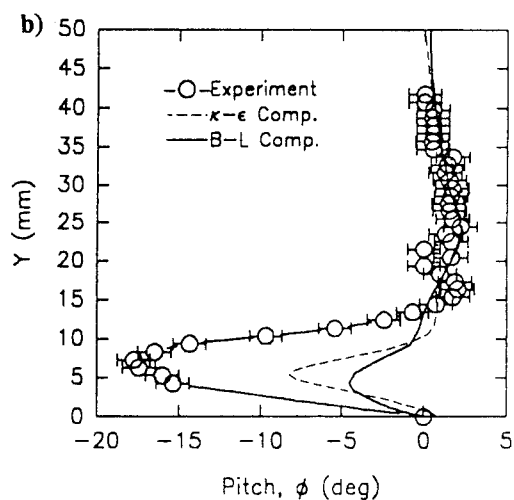
Figure 18 Comparison of the pitch angle variation in the Y direction at a) X = 0 mm and b) X = ± 5 mm.

AIAA 94-2274

MEASUREMENTS AND COMPUTATION OF THE TRIPLE SHOCK WAVE/TURBULENT BOUNDARY LAYER INTERACTION

T.J. Garrison and G.S. Settles
Pennsylvania State University, University Park, PA

C.C. Horstman
NASA-Ames Research Center, Moffett Field, CA

25th AIAA Fluid Dynamics Conference
June 20-23, 1994 / Colorado Springs, CO

MEASUREMENTS AND COMPUTATION OF THE
TRIPLE SHOCK WAVE/TURBULENT BOUNDARY LAYER INTERACTION

T.J. Garrison[*] and G.S. Settles[**]
Dept. of Mechanical Engineering, Pennsylvania State University
C.C. Horstman[‡]
NASA-Ames Research Center

ABSTRACT
A joint experimental and computational study has investigated the flowfield structure created by three crossing oblique shock waves interacting with a turbulent boundary layer. Such an interaction is of practical importance in the design of high-speed sidewall-compression inlets. The interaction is created by a test model consisting of two vertical sharp fins mounted at 15 degrees angle-of-attack to a horizontal flat plate. A third compression surface of 10 degree angle is mounted to the plate between the two vertical fins. The Mach 3.85 flowfield is examined experimentally through kerosene lampblack and Planar Laser Scattering (PLS) visualizations. The results are used to develop a flowfield model of the interaction structure. This structure is found to consist of a complex wave pattern overlying a viscous separated region. The presence of the 10° compression ramp reduces the severity of the boundary layer separation compared to interactions created by the two fins alone. Additionally, the experimental flowfield data are compared with a computational solution using a modified κ-ε (Rodi) turbulence model. A comparison of the results shows that, despite the complexity of the flowfield, the computed solution shows good overall agreement with the experimental data.

INTRODUCTION
Over the past several years there has been an ongoing research effort to understand the flowfield created by two crossing oblique shock waves interacting with a turbulent boundary layer, as shown in Fig. 1. A major objective for studying this flowfield is to gain a basic understanding of the viscous/inviscid interactions within a generic high-speed sidewall-compression inlet. The geometry shown in Fig. 1, commonly referred to as a crossing-shock interaction, simulates an inlet with compression surfaces on the sides of the inlet only. A great deal has been learned about this interaction through a range of experimental[1-15] and computational[16-22] investigations. The most prominent feature of the crossing-shock interaction is the large separated flow region it produces on the interaction centerline (c.f. Refs. 9,14).

Of course, practical inlets likely involve more than just side-wall compression. Given the knowledge base formed by these crossing-shock studies, it is now possible to add additional features to the generic inlet.

This paper addresses the flowfield generated by adding a compression ramp to the existing crossing-shock model. The model geometry used to generate this interaction is shown in Fig. 2. In this geometry, a third compression surface is added to the generic inlet, making it more characteristic of realistic inlet designs.

There are two primary objectives of the present paper. The first is to present the experimentally obtained flow visualization results of the triple-shock interaction along with a discussion of the main flowfield features. The second objective is to compare the experimental results with a recently-completed computational prediction of the triple-shock flowfield. Such a comparison is useful to assess the capabilities of current CFD codes as well as to provide additional insight into the triple-shock interaction.

The joint experimental and computational results described herein represent the first known investigation of the triple-shock flowfield. Because no experimental or computational data of any kind have been available on this interaction, the following results give valuable insight into the nature of the flow and provide a framework for further studies.

DESCRIPTION OF EXPERIMENTS
Wind Tunnel Facility and Test Conditions
The experiments were performed in the Penn State Gas Dynamics Laboratory's Supersonic Wind Tunnel Facility, which is an intermittent blowdown tunnel with a test section size of 15x17x60 cm. This facility has a unique variable Mach number capability over the range from Mach 1.5 to 4.0 by way of an asymmetric sliding block nozzle. The experiments described in this paper were carried out at a Mach number of 3.85, with a stagnation pressure of 1500

---

[*]Graduate Research Assistant, Student Member AIAA.

[**]Professor of Mechanical Engineering and Director, Gas Dynamics Laboratory, Associate Fellow AIAA.

[‡]Senior Scientist, Associate Fellow AIAA.

terms of the reflection of a single-fin interaction from an inviscid wall.[8-10,14]

Because the triple-shock interaction shown in Fig. 2 is also symmetric, the same reflection-plane analysis can be used to understand its structure. Whereas the crossing-shock interaction was treated as the reflection of a single-fin interaction, the triple-shock interaction can be thought of as the reflection of a *corner flow* interaction. Thus, it is important to understand the structure of the corner flow which undergoes the reflection process. The remainder of this section reviews the main features of the corner flow which makes up the triple-shock interaction.

The supersonic flowfield created in the corner of two intersecting wedges has received a great deal of study over the past several decades. Charwat and Redekeopp[27] were the first to develop a flowfield model of the inviscid wave structure in a corner. Numerous additional investigations have been performed for a range of incoming Mach numbers and wedge angles. However, because past studies did not addresses the particular Mach number and wedge angle combination of interest to the present investigation, PLS visualizations of the corner flow were performed as part of the current study.

Fig. 3 shows a PLS image for a corner flow created by a 15° fin and a 10° ramp in a Mach 3.85 freestream flow. This image, taken 11.1 cm from the combined fin and ramp leading edge, is to scale and shows the shock wave structure in a plane normal to the freestream flow direction (i.e. referring to Fig. 1b, in an X-Y plane). Fig. 4 shows a schematic of the flowfield features revealed in the PLS image of Fig. 3. Qualitatively, the interaction structure shown in Figs. 3 and 4 is in good agreement with that of previous corner flow models (c.f. Ref. 28). The flowfield within the corner consists of the inviscid shocks generated by the fin and ramp joined by a corner shock. This corner shock is the result of an irregular (i.e. Mach) intersection of the two inviscid shocks. Also, emanating from the ends of the corner shock are two embedded shock waves. These embedded shocks both bifurcate into a separation and rear shock due to their interactions with the boundary layers on the fin and ramp surfaces. In future discussions it will be useful to distinguish between these two embedded shock systems. Thus, they have been identified in Fig. 4 based on whether they are generated by the fin or ramp surface. Beneath the two bifurcated shock systems are two separated flow regions.

Additionally, within the corner interaction there are four triple points and four corresponding sliplines. All four of these sliplines asymptote together and terminate at the ramp-fin intersection.

As already stated, the triple-shock interaction can be considered as the reflection of this corner flow from the reflection (i.e. symmetry) plane. However, it should be noted that, insofar as the structure of the corner flow is already complex, its reflection can be expected to be still more complex in structure.

RESULTS
Triple-Shock Limiting Streamline Pattern

Fig. 5a) shows a kerosene-lampblack surface flow visualization for the triple-shock interaction. An annotated tracing of the this pattern is given in Fig. 5b) for clarity. Upstream, near the fin and ramp leading edges, the surface pattern near each fin is identical to that of a corner-flow interaction (c.f. Ref. 28). The prominent features in the surface pattern include the upstream influence line (UI), the primary attachment line (PA), and the primary separation line (PS). The location of the inviscid fin shock (IFS) is also shown for reference. In the upstream portion of the flow, the surface features appear as straight lines due to the conical nature of the corner flow. These features remain as straight conical rays until the point at which the two upstream influence lines meet, whence the various lines begin to deviate significantly from conical behavior. This point marks the location at which the two corner flows begin to sense the presence of one another.

Following the primary separation lines (PS) further downstream in Fig. 5b), they are observed to initially converge toward the interaction centerline and then diverge from it. Upon reaching a local maximum distance from the centerline, the separation lines again converge slowly toward it. This same converging-diverging-converging separation-line pattern was observed previously in surface traces of crossing-shock interactions[9,10] such as the one shown in Fig. 6. The trace shown in Fig. 6 is for the same fin angles (15°) and incoming Mach number (3.85) as the triple-shock trace shown in Fig. 5a).

In Fig. 5a), near the interaction centerline, between the two primary separation lines, the surface streamlines diverge from the centerline and converge upon the separation lines on either side, indicating a line of flow attachment on the interaction centerline. Again, this same behavior has been observed in studies of crossing-shock interactions.

It is useful to compare in more detail the triple-shock trace shown in Fig. 5 to the corresponding crossing-shock trace of Fig. 6. While the basic features of these patterns are similar, it is clear that details in the vicinity of the interaction centerline are distinctly different. The most interesting aspect of the comparison is that the spanwise extent of the surface features near the centerline is much smaller in the triple-shock interaction. In fact, the surface pattern for the triple-shock interaction is very similar to that of a *weaker*, Mach 3, $\alpha = 11°$ crossing-shock interaction (c.f. Refs. 10,14). Because it has been shown that the topological features near the interaction centerline are associated with the separation of the incoming boundary layer,[10] it appears that the separation caused by the triple-shock interaction is less severe than that caused by the crossing-shock interaction of equal fin angles, despite the fact that the overall compression is greater in the triple-shock configuration. This observation is very important, since the major problem identified with the

to the finite height of the fin which generates it. Thus, for frames g) and beyond the fin height influences the interaction and renders it no longer semi-infinite. The curvature of the inviscid fin shock influences its reflection, giving rise to a more complex reflected wave pattern than would be so for semi-infinite fin heights.

Frame g) marks the approximate streamwise location at which the reflection of the incident corner flow from the reflection plane is complete. (The inviscid fin shocks continue to reflect due to their curvature.) The reflected wave system then propagates out toward the fin surface, as shown in frames h) and i). Provided the fins are long enough, another sequence of reflections will occur at the fin surface with the added complexity of viscous effects associated with the fin boundary layer. We have made no attempt to model that occurrence here.

In addition to the wave structure just described, it is also of interest to follow the evolution of the sliplines and separated flow regions. As the corner flow shock structure propagates toward the reflection plane, the sliplines originating at the four triple points extend into the fin-ramp junction. However, it is observed that, once a given triple point reflects from the reflection plane, its corresponding slipline then grows outward from the interaction centerline (c.f. frame g). The sliplines originally created during propagation toward the centerline appear to be "washed-out" as the wave structure propagates back toward the fin.

Through much of the upstream portion of the interaction, the separated flow regions on the fin and ramp surfaces are obscured in the PLS images of Fig. 8. The top of the separated region on the ramp is first visible in frame e) of the PLS images, whereas the separated regions on the fin surfaces remain outside the camera field of view in all the frames. Thus, the size and location of the fin separated region shown in Fig. 9 are approximate. The separated regions on the fins are very small and are located close to the surface. This is a result of the extremely thin boundary layer on the fins compared to that on the ramp. (The ramp boundary layer originates at the leading edge of the flat plate, 21.3 cm ahead of the fin leading edges.) Also, the ramp embedded shock wave which interacts with the fin boundary layer is weaker due to the 10° deflection angle of the ramp compared to the 15° fin angle.

Fig. 10a) shows a PLS image taken at the trailing edge of the fins and ramp. While the wave structure is difficult to see at this plane, the image shows the size and shape of the separated region on the ramp surface. It is useful to compare this image with an image taken at the same location without the ramp in place (i.e. for a crossing-shock interaction) as shown in Fig. 10b). The two images in Fig. 10 are to the same scale, although the crossing-shock image has been shifted vertically to align the locations of the horizontal model surfaces.

Fig. 10 clearly shows that the size of the separated flow region is significantly smaller in the triple shock interaction, despite the fact that the overall compression is greater for this configuration. This result is consistent with that observed in the previous analysis of the surface flow pattern. Comparing the areas of the separated regions in Fig. 10 shows that the triple-shock separated flow region is approximately 45% smaller than that of the crossing-shock flow.

It is important to understand why the added compression surface in the triple-shock geometry reduces the severity of the boundary layer separation over that without the compression ramp. In the triple-shock case, provided the ramp angle is less than that required for incipient separation, the compression ramp is able to "pre-compress" the incoming boundary layer without causing it to separate. (For a compression ramp at Mach 3.85, incipient turbulent boundary layer separation occurs at a ramp angle of $\phi \approx 20°$.) Because the Mach number is reduced through the ramp shock, the strength of the viscous interaction caused by the fin shocks is also reduced compared to the case without the ramp. Thus, in the triple-shock interaction the fin separation and rear shocks are significantly weaker than those of the corresponding crossing-shock interaction, hence, the size of the separated region beneath these waves is significantly smaller. In effect, though the triple-shock configuration adds more compression, this compression is distributed in such a way as to reduce the potential for boundary layer separation. This observation suggests that modifications to the crossing-shock geometry might be made to reduce the extent of the separated region and increase the overall inlet compression. It also demonstrates that higher overall inlet compression does not necessarily increase the severity of boundary layer separation problems.

Comparison with Computed Results

The remainder of this section compares the previously described experimental flowfield to that obtained from the computation. For brevity, the experiment and computation are compared only at two planes within the interaction. Similar results are found throughout the entire interaction.

Fig. 11 shows the computed static pressure distribution at $Z/\delta_\infty = 20.1$, which corresponds to the location of frames b) in Figs. 8 and 9. For comparison, the experimental flowfield model from Fig. 9 has been overlaid on the right half of the computed pressure distribution. Overall, there is relatively good agreement between the computation and experiment, with the computed pressure contours reasonably matching the experimental wave locations within the resolution of the former. However, unlike the experimental PLS images, the shock waves in the computation are poorly captured, the pressure rise across these waves being spread out over a significant distance.

The computed static pressure contours and experimental flowfield structure at $Z/\delta_\infty = 25.7$ are compared in Fig. 12. This Z location corresponds to frames f) of Figs. 8 and 9. At this location, the reflection of the incident corner flow is nearly complete. Again, there is

5

11)Kussoy, M.I., and Horstman, K.C., "Intersecting Shock-Wave/Turbulent Boundary-Layer Interactions at Mach 8.3," NASA TM 103909, Feb. 1992.

12)Kussoy, M.I., Horstman, K.C., and Horstman, C.C., "Hypersonic Crossing Shock-Wave/Turbulent-Boundary-Layer Interactions," AIAA Paper 93-0781, Jan. 1993.

13)Forkey, J., Cogne, S., Smits, A., Bogdonoff, S., Lempert, W.R., and Miles, R.B., "Time-Sequenced and Spectrally Filtered Rayliegh Imaging of Shock Wave and Boundary Layer Structure for Inlet Characterization," AIAA Paper 93-2300, June, 1993.

14)Garrison, T.J., *The Interaction Between Crossing-Shock Waves and a Turbulent Boundary Layer*, Ph.D. Thesis, The Pennsylvania State University, M.E. Dept., Aug. 1994.

15)Garrison, T.J., Settles, G.S., Narayanswami, N., Knight, D.D., and Horstman, C.C., "Comparison of Flowfield Surveys and Computations of a Crossing-Shock Wave/Boundary Layer Interaction," AIAA Paper 94-2273, June 1994.

16)Gaitonde, D., and Knight, D.D., "Numerical Experiments on 3-D Shock Wave-Boundary Layer Interaction Generated by a Sharp Fin," AIAA Paper 88-0309, Jan. 1988.

17)Reddy, D.R., "3-D Navier-Stokes Analysis of Crossing, Glancing Shocks/Turbulent Boundary Layer Interactions," AIAA Paper 91-1758, June 1991.

18)Narayanswami, N., Knight, D., Bogdonoff, S.M., and Horstman, C.C., "Interaction Between Crossing Oblique Shocks and a Turbulent Boundary Layer," *AIAA Journal*, vol.30, no. 8, Aug. 1992.

19)Narayanswami, N., Knight, D.D., and Horstman, C.C., "The Investigation of a Hypersonic 3-D Crossing Shock/Turbulent Boundary Layer Interaction," *Shock Waves*, Vol. 3, No. 1, 1993.
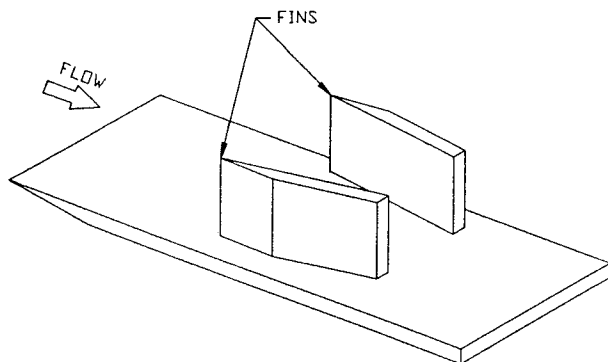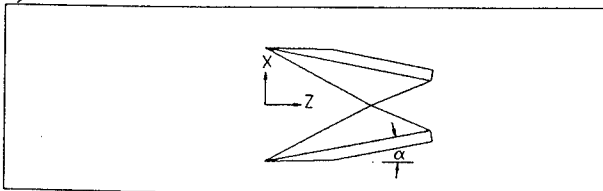
20)Narayanswami, N., Horstman, C.C., and Knight, D.D., "Numerical Simulation of Crossing Shock/Turbulent Boundary Layer Interaction at Mach 8.3 - Comparison of Zero- and Two-Equation Turbulence Models," AIAA Paper 93-0779, Jan. 1993.

21)Narayanswami, N., Horstman, C.C., and Knight, D.D., "Computation of Crossing Shock/Turbulent Boundary Layer Interactions at Mach 8.3," *AIAA Journal*, vol. 31, no. 8, Aug. 1993.

22)Gaitonde, D., and Shang, J.S., "Calculations on a Double-Fin Turbulent Interaction at High Speed," AIAA Paper 93-3432, Aug. 1993.

23)Settles, G.S., and Teng, H.Y., "Flow Visualization Methods for Separated Three-Dimensional Shock Wave/Turbulent Boundary Layer Interactions," *AIAA Journal*, Vol. 21, March 1983.

24)Rubesin, M. and Rose, W., "The Turbulent Mean Flow Reynolds-Stress and Heat Flux Equations in Mass Averaged Dependent Variables," NASA TMX 62248, 1973.

25)Rodi, W., "Experience with Two-Layer Models Combining the κ-ε with a One-Equation Model Near the Wall," AIAA Paper No. 91-0216, Jan. 1991.

26)MacCormack, R.W., "A Numerical Method for Solving the Equations of Compressible Viscous Flow", *AIAA Journal*, Vol. 20, no. 9, Sept. 1982.

27)Charwat, A.F., and Redekeopp, L.G., "Supersonic Interference along the Corner of Intersecting Wedges," *AIAA Journal*, Vol. 5, No. 3, March 1967.

28)West, J.E., and Korkegi, R.H., " Supersonic Interaction in the Corner of Intersecting Wedges at High Reynolds Numbers," *AIAA Journal*, Vol. 10, No. 5, May 1972.
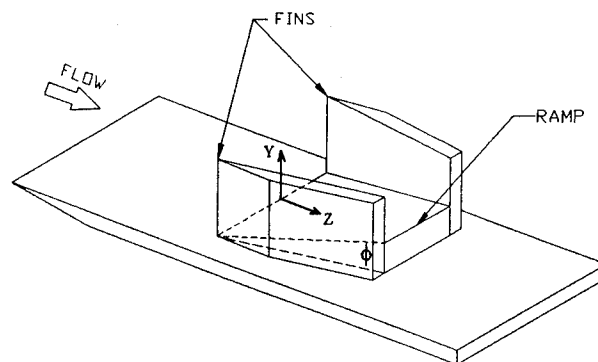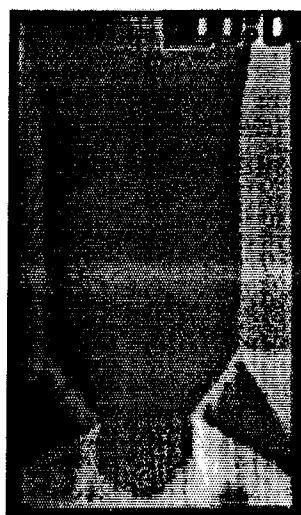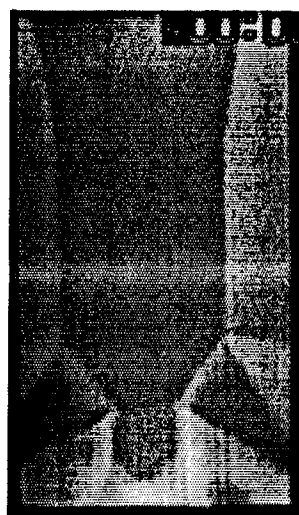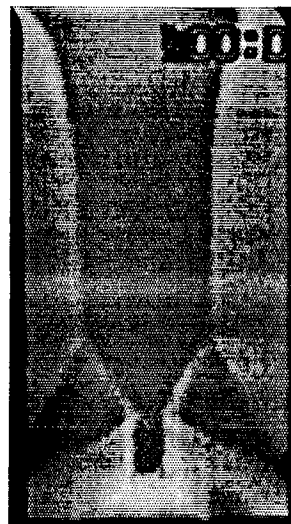
a)

b)

Figure 1 **Experimental crossing-shock model, a) perspective view, b) top view.**

Figure 2 Experimental triple-shock model
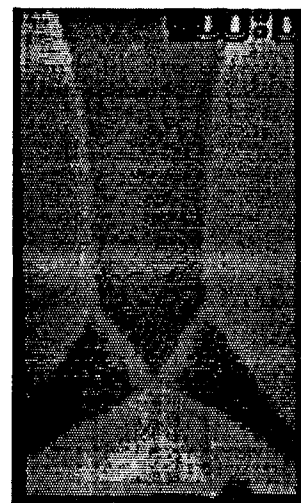
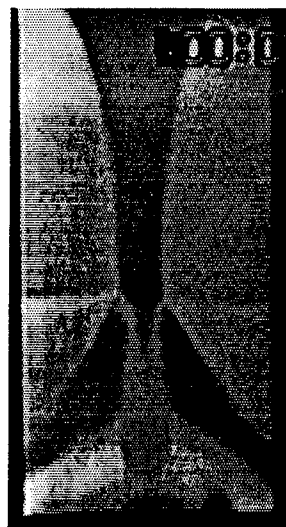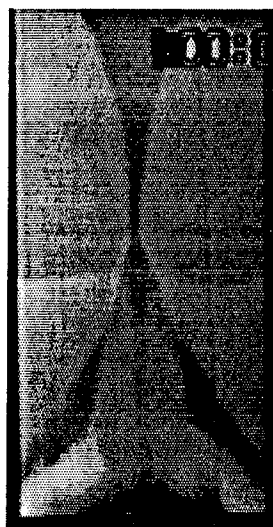a) $Z/\delta_\infty = 19.1$ b) $Z/\delta_\infty = 20.1$ c) $Z/\delta_\infty = 21.3$ d) $Z/\delta_\infty = 22.2$
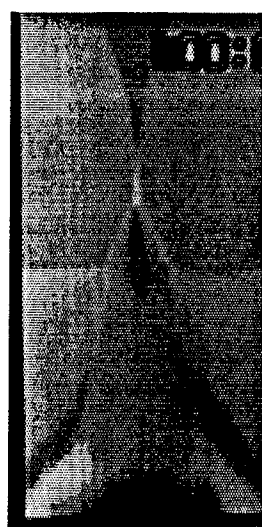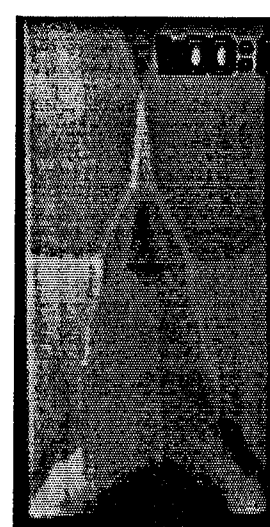
e) $Z/\delta_\infty = 24.2$ f) $Z/\delta_\infty = 25.7$ g) $Z/\delta_\infty = 26.7$ h) $Z/\delta_\infty = 27.7$

i) $Z/\delta_\infty = 29.3$

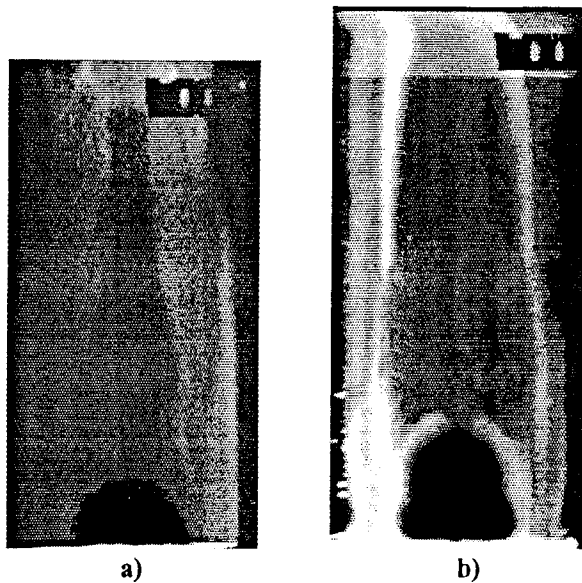Figure 8 PLS images for a $M_\infty = 3.85$, $\alpha = 15°$, $\phi = 10°$ triple-shock interaction.

9

Figure 10 PLS images at $Z/\delta_\infty = 36.3$ for a a) triple-shock interaction and b) crossing-shock interaction.
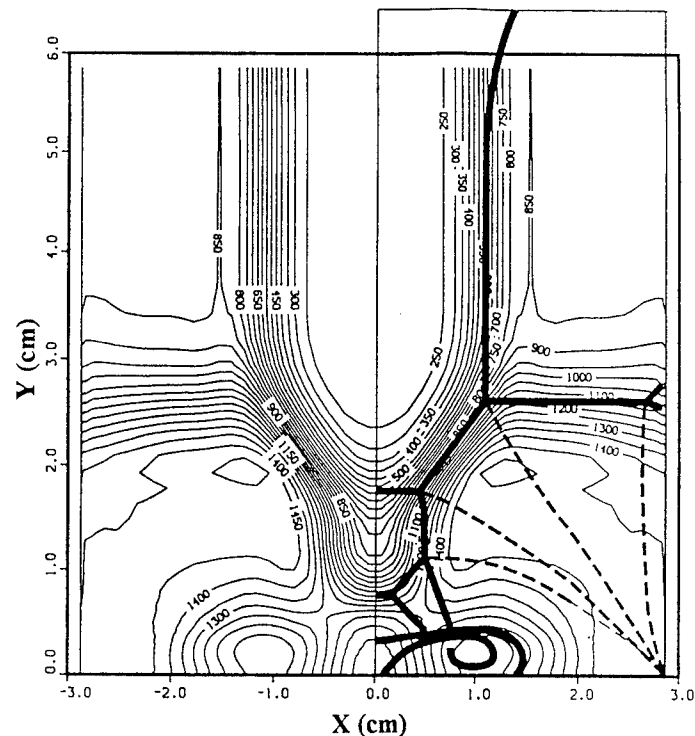

Figure 11 Comparison of the computed static pressure contours (kPa) with the experimental flowfield model at $Z/\delta_\infty = 20.1$.
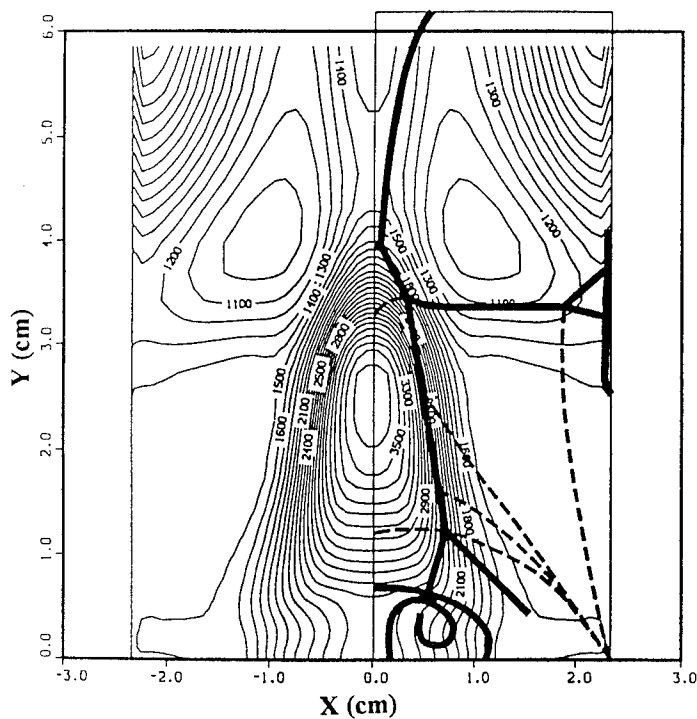

Figure 12 Comparison of the computed static pressure contours (kPa) with the experimental flowfield model at $Z/\delta_\infty = 20.1$.
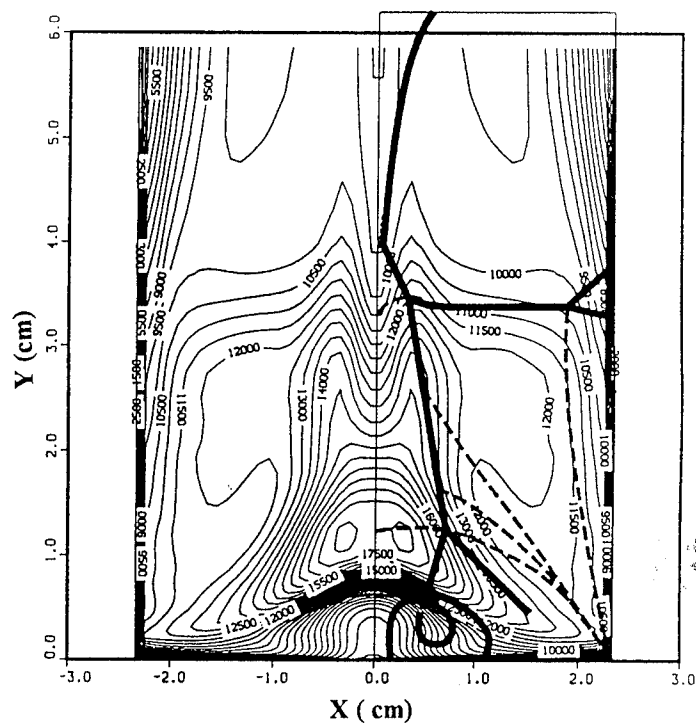

Figure 13 Comparison of the computed pitot pressure contours (kPa) with the experimental flowfield model at $Z/\delta_\infty = 25.7$.